Microporous and Mesoporous Materials 372 (2024) 113098

Contents lists available at ScienceDirect

Microporous and Mesoporous Materials

journal homepage: www.elsevier.com/locate/micromeso

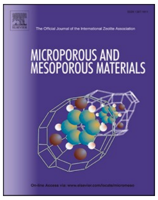

Zeolite Y-based catalysts for efficient epoxidation of R-(+)-Limonene: Insights into the structure-activity relationship

Luis A. Gallego-Villada [a,b,**], Päivi Mäki-Arvela [b], Narendra Kumar [b], Edwin A. Alarcón [a], Zuzana Vajglová [b], Teija Tirri [b], Ilari Angervo [c], Robert Lassfolk [d], Mika Lastusaari [e], Dmitry Yu Murzin [b,*]

[a] *Environmental Catalysis Research Group, Chemical Engineering Faculty, Universidad de Antioquia, Medellín, Colombia*
[b] *Laboratory of Industrial Chemistry and Reaction Engineering, Johan Gadolin Process Chemistry Centre, Åbo Akademi University, Henriksgatan 2, 20500, Turku/ Åbo, Finland*
[c] *Wihuri Physical Laboratory, Department of Physics and Astronomy, FI-20014, University of Turku, Finland*
[d] *Laboratory of Molecular Science and Engineering, Åbo Akademi University, Finland*
[e] *University of Turku, Department of Chemistry, FI-20014, Turku, Finland*

ARTICLE INFO

Keywords:
Zeolite Y
Hierarchical zeolite
Epoxidation
Limonene
Catalyst

ABSTRACT

Parent, hierarchical, and metal-modified hierarchical zeolite Y were investigated as heterogeneous catalysts in the R-(+)-limonene epoxidation, a catalytic route for synthesizing precursors of bio-polycarbonates, an alternative to isocyanate polyurethanes. The fresh catalysts underwent detailed characterization using XRD, N_2 physisorption, TEM, SEM-EDX, pyridine-FTIR, NH_3-TPD, CO_2-TPD, UV–Vis-DRS, and solid-state NMR. Spent materials were investigated by TPO-MS and TGA, confirming low coke formation on the catalytic surface. The most active material was K–Sn-modified dealuminated zeolite Y, reflected in a high turnover frequency (TOF) of 96 h^{-1}. This material exhibited the lowest Brønsted to Lewis acidity ratio (0.1), the highest mesoporosity fraction (43%), and the lowest total surface area (465 $m^2\ g^{-1}$). Aprotic polar solvents with high polarity and medium donor capacity appeared suitable for limonene epoxidation. Limonene conversion of ca. 97% was reached at 70 °C, H_2O_2: limonene molar ratio = 7, and acetonitrile as a solvent, while selectivity to total monoepoxides exhibited values up to 96% under different reaction conditions. Hydration of internal epoxides to limonene diol was favored at high temperatures and high H_2O_2/limonene molar ratios. The efficiency of H_2O_2 reached maximum values of about 85% at low H_2O_2 amounts, while no significant influence was observed for temperature, catalyst amount, and the initial concentration of limonene. A plausible reaction mechanism was proposed for the R-(+)-limonene epoxidation with H_2O_2 based on the experimental findings.

1. Introduction

Molecular sieves refer to crystalline materials with a variety of compositions that exhibit shape-selective adsorption and reaction properties [1]. Zeolites, a specific type of molecular sieve, are crystalline aluminosilicates with a three-dimensional framework structure that creates uniformly sized pores of molecular dimensions, ranging from angstroms (Å) to a couple of nanometers (nm) [2]. These pores selectively adsorb molecules that fit easily within their confines while excluding larger molecules [3]. The remarkable and highly exploitable properties of zeolitic materials, including their ion-exchange capacity, strong acidic sites, large surface area, high thermal stability, sorption capacity, shape selectivity, catalytic activity, and their role as hosts in advanced materials, are primarily governed by their unique structures [4]. However, the microporosity of zeolites limits their applicability for transforming relatively large organic molecules due to the pore diffusion limitations imposed by the microporous network structure [5]. To overcome these limitations, various synthesis methods have been employed to produce zeolites with mesoporous (2–50 nm) [6,7] and macroporous (> 50 nm) [8,9] dimensions, which are generally preferred and well-known as hierarchical zeolites.

Zeolites are extensively used in applications of gas separation [10,

---

* Corresponding author.
** Corresponding author. Environmental Catalysis Research Group, Chemical Engineering Faculty, Universidad de Antioquia, Medellín, Colombia.
E-mail addresses: alfonso.gallego@udea.edu.co (L.A. Gallego-Villada), dmitry.murzin@abo.fi (D.Y. Murzin).

https://doi.org/10.1016/j.micromeso.2024.113098
Received 24 January 2024; Received in revised form 6 March 2024; Accepted 20 March 2024

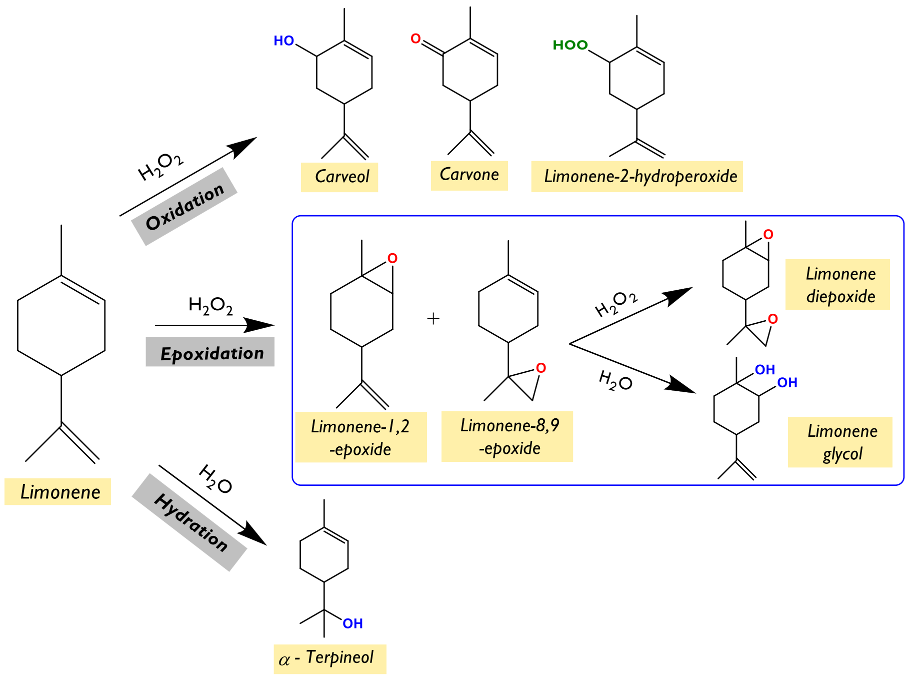

Fig. 1. Reaction pathways for the catalytic transformation of limonene via oxidation.

11] and adsorption [12–14], but also as heterogeneous catalysts in different areas such as the petrochemical industry [15–17], the production of biofuels [18–21], and the synthesis of fine chemicals [22–27]. Fine chemistry represents one of the most important industries with a projected estimated market of ca. US \$ 185 $\times$ 10^3 million in 2023, covering perfumes, intermediates in the synthesis of active pharmaceutical ingredients (APIs), and various green chemicals [28]. Zeolites as heterogeneous catalysts offer the advantage of being relatively inexpensive, easy to recover, and recyclable. These aspects are closely aligned with the objectives of green chemistry, aiming to minimize or, ideally, eliminate waste generation in chemical processes. As a result, there has been a growing awareness of the importance of green chemistry metrics in catalysis studies, making the research of efficient heterogeneous materials as catalysts imperative [29].

Limonene is a monoterpene ($C_{10}H_{16}$) with two double bonds (ring and external), which is typically the major constituent of essential oils derived from various biomass found in citrus fruit peels, such as lemons, limes, grapefruits, mandarins, and oranges. The citrus fruit production in 2021 was estimated at 162 million tons, being China (28.8%) the top country in worldwide production, followed by Brazil, India, Mexico, and Spain [30]. The citrus waste during juice production is about 50%, which includes peels, seeds, pomace, and wastewater [31]. Specifically, about 15 million tons of orange peel waste are generated annually where 60,000 metric tons correspond to extracted R-(+)-limonene [32,33].

Limonene finds extensive use in various industrial applications, serving as a flavor and fragrance additive in cleaning and cosmetic products, food, beverages, and pharmaceuticals. Additionally, it plays a crucial role in the manufacturing of resins, acts as a wetting and dispersing agent, and contributes to the insect control. Moreover, limonene has been employed as a sorption promoter or accelerant to enhance transdermal drug delivery and works by penetrating the skin, effectively reducing barrier resistance in a reversible manner [34]. On the other hand, limonene is an important precursor in the synthesis of oxygenated compounds such as monoepoxides (*cis* and *trans* of internal and external configurations) and diepoxides (*cis* and *trans*). Recently, these epoxides products have been considered promising building blocks in the production of bio-polycarbonates which have shown attractive thermal and optical properties [35–40]. Limonene-based carbonates offer a versatile option for producing non-isocyanate polyurethanes (NIPUs) with properties comparable to those of commercially available polyurethanes, without the utilization of toxic isocyanates in their synthesis [41,42].

The reaction pathways of limonene with H_2O_2 as the oxidizing agent (Fig. 1) can yield various products depending on the catalyst, the solvent, and the reaction conditions such as the H_2O_2: limonene ratio, H_2O_2 concentration, amount of solvent, and temperature. The synthesis of allylic products, such as carveol and carvone, has been favored over epoxides and hydration products using V/MCM-41 [43], nanoporous carbon [44], Ti/SBA-15 [45], and Cu/MCM-41 [46] as heterogeneous catalysts and H_2O_2 as an oxidizing agent, reaching selectivities about 61.5%, 65.2%, 45.6% and 41.3%, respectively, but with low limonene conversions (<42%), under the tested reaction conditions. More active systems with H_2O_2 have been reported based on zeolite Y immobilized with heterogenized binuclear V(IV)O ([VO(*sal₂bz*)]₂-Y) and Fe(II) ([Fe (*sal₂bz*) (H_2O)₂]₂-Y) complexes [47] with limonene conversions larger than 80% and selectivities to allylic products of ca. 49.0% and 46.0%, respectively, using acetonitrile as a solvent and 80 °C for 24 h. Furthermore, limonene glycol was observed as the main byproduct with these catalysts, reaching selectivity of 39.0% and 43%, respectively. A Keggin heteropolyacid ($H_3PMo_{12}O_{40}$) supported on SiO_2 has been reported as a catalyst in a solvent-free system, with TBHP as an oxidizing agent, showing limonene conversion of 91% and selectivity to glycol of ca. 47.0% [48].

Many heterogeneous catalytic systems yield limonene monoepoxides as the main products, which are based on oxides such as MgO [49], WO_3/SiO_2 [50], γ-AlO(OH)-nanorods [51], and W/SiO_2 [52]; hybrid composites such as a Co-substituted phosphomolybdate acid encapsulated in the UiO-66 framework (PMo11Co@UiO-66) [53], an organic-inorganic hybrid based on MoO_3 chains with 2,2′-biimidazole ligands ([MoO_3(biim)]) [54], and Mg/Al hydrotalcites-Au nanoparticles [55]; complexes-based catalysts such as a terpyridine-based Mo(VI) complex on manganese ferrite ($MnFe_2O_4$/Phttpy-MoO_2) [56], a 5-(2-pyridyl)tetrazolate complex of Mo(VI) (MoO_3(Hpytz)) [57], and two layered double hydroxides ZnAl-LDH and MgAl-LDH functionalized with bis(4-HOOC-phenyl)-acenaphthenequinonediimine (BIAN) [58]; MOFs-based catalysts such as Mo/Hf-MOF [59] and Zn/Co-MOF [60];

Table 1
Description of the catalytic materials.

Entry	Catalyst	Description
1	HY	H–Y-30
2	HYD	H–Y-30-DA
3	SnHYD1	2 wt% Sn–H–Y-30-DA
4	KSnHYD1	K-2 wt% Sn–H–Y-30-DA
5	SnHYD2	15.8 wt% Sn–H–Y-30-DA
6	KSnHYD2	K-15.8 wt% Sn–H–Y-30-DA

DA refers to the dealumination procedure.

activated carbons as Ru/Darco-G60 [61]; mesoporous materials such as Co/SBA-16 [62], Ni/SBA-16 [62], TiO_2/SiO_2–Mn [63], Ti/SBA-16 [64, 65], Mo-TUD-1 [66], and Ti/KIT-6 [67]; and microporous materials such CoO_x/mordenite [68]. The ZnAl-LDH-BIAN-MoI_2 catalyst has been reported to exhibit the highest selectivity for limonene monoepoxides (97%) with a remarkable limonene conversion (94%) when using TBHP as the oxidizing agent and toluene as the solvent at 110 °C for 24 h [58]. The [MoO_3(biim)] catalyst is another promising material, which yielded limonene conversion of 97% with selectivity of 80% towards monoepoxides when TBHP and α, α, α-trifluorotoluene (TFT) were employed as the oxidant and the solvent, respectively.

Despite a wide range of catalytic materials reported in the literature, mesoporous zeolitic materials (hierarchical zeolites) with appealing morphological, textural, and acidic properties have not been extensively explored as heterogeneous catalysts for the valorization of limonene towards its monoepoxides. Herein, this study aims to investigate the limonene epoxidation route using H_2O_2 as a green oxidizing agent over hierarchical zeolite Y-based catalysts. The research will focus on studying the physicochemical properties of the catalysts, including crystalline phases, morphology, textural properties, acidity, and environment of the species in the zeolitic materials, and correlating them with the catalytic performance. The effect of various parameters such as the solvent nature, substrate initial concentration, catalyst loading, oxidant/substrate feed ratio, reaction temperature, and catalyst stability will be evaluated.

2. Materials and methods

2.1. Reagents

Commercial materials were used in the experiments without further processing. Reagents for the synthesis of catalysts were UHY zeolite (CBV 720, SiO_2/Al_2O_3 molar ratio = 30, Zeolyst International), nitric acid solution (HNO_3, 70 wt %, Fischer Scientific), tin (IV) chloride pentahydrate ($SnCl_4·5H_2O$, 98 wt %, Sigma-Aldrich), triethylamine (TEA, 99 wt %, Alfa Aesar), and potassium chloride (KCl, ≥ 99.5 wt %, Merck). Reagents for the catalytic tests were R-(+)-limonene ($C_{10}H_{16}$, 97 wt %, Sigma-Aldrich), hydrogen peroxide solution (H_2O_2, 30 wt %, Sigma-Aldrich), acetonitrile (CH_3CN, gradient grade for liquid chromatography, Merck), *N*–N-dimethylformamide (DMF, ≥ 99.5 wt %, VWR Chemicals), ethyl acetate ($C_4H_8O_2$, ≥ 99.5 wt %, Sigma-Aldrich), dimethyl carbonate (DMC, 99 wt%, Sigma-Aldrich), cyclohexane (99.9 wt%, Thermo Scientific), tetrahydrofuran (THF, 99.9 wt%, Sigma-Aldrich), and 2-butanol (99 wt%, Acros Organics). Reagents used as standards for the quantification through the multipoint calibration curves were *cis*-(−)-limonene oxide ($C_{10}H_{16}O$, 98 wt %, Sigma-Aldrich), *trans*-limonene-1,2-epoxide ($C_{10}H_{16}O$, 97.5 wt %, Sigma-Aldrich), (4R, 8RS)-limonene-8,9-epoxide ($C_{10}H_{16}O$, 95 wt %, Biosynth), D-dihydrocarvone ($C_{10}H_{16}O$, ≥ 97 wt %, mixture of isomers, Sigma-Aldrich), L-carveol ($C_{10}H_{16}O$, mixture of *cis* and *trans*, ≥ 95 wt %, Sigma-Aldrich), R-(−)-carvone ($C_{10}H_{14}O$, 98 wt %, Sigma-Aldrich), α-terpineol ($C_{10}H_{18}O$, ≥ 95 wt %, Sigma-Aldrich), dipentene dioxide ($C_{10}H_{16}O_2$, 95 wt %, Sigma-Aldrich), and (1*S*,2*S*,4*R*)-(+)-limonene-1,2-diol (≥ 97 wt %, Sigma-Aldrich). Reagents for the quantification of H_2O_2 concentration were ammonium cerium (IV) sulfate solution ($Ce(NH_4)_4(SO_4)_4$, 0.1 mol L^{-1}, VWR Chemicals), ferroin solution indicator (1,10-phenanthroline iron (II) sulfate, VWR Chemicals) and sulfuric acid (H_2SO_4, 95–98 wt %, Fluka).

2.2. Synthesis of catalysts

The catalysts were prepared following the procedure outlined by Jimenez-Martin et al. [69] with some modifications (Table 1). Commercial CBV 720 zeolite (H–Y-30), designated as HY, was dealuminated treating it with a 10 M aqueous HNO_3 solution (20 mL g^{-1} of zeolite) for 1 h at room temperature with continuous stirring (120–150 rpm). The resulting solid was recovered via filtration, washed thoroughly with distilled water until reaching a neutral pH, and subsequently dried at 105 °C overnight. This dealumination procedure was repeated twice to ensure the effective removal of a substantial amount of the initial aluminum loading. The resulting material was denoted as HYD.

Sn was introduced by combining $SnCl_4·5H_2O$ (2 or 15.8 wt % Sn) with 250 mL of distilled water, followed by stirring the suspension at room temperature (120–150 rpm) for 5 h. The objective of extending the contact time was to enhance the diffusion of the tin source within the porous structure of the zeolite, fostering a close interaction between the metal precursor and the zeolite support. Subsequently, TEA was introduced with stirring (120–150 rpm) for 2 h to chemically facilitate Sn incorporation, maintaining a TEA: $SnCl_4·5H_2O$ molar ratio of 4. During this stage, TEA acted as an activator for the grating of the metal, activating the silanol groups in the dealuminated zeolite. These active groups readily attracted the tin species, resulting in the formation of Sn–*O*–Si bonds. Simultaneously, TEA acted as a neutralizer for the hydrogen chloride generated in the reaction, leading to the formation of a soluble adduct in water, such as triethylamine hydrochloride. The zeolite was subsequently recovered by filtration and dried at 105 °C before undergoing calcination in static air through a stepwise procedure. This involved heating the catalyst from room temperature to 250 °C for 75 min, maintaining this temperature for 40 min, raising the temperature to 550 °C within 120 min, holding it for 240 min, and finally cooling the catalyst to 25 °C over 100 min. The resulting solid was designated as SnHYDx, with x = 1 for a Sn loading of 2 wt % and x = 2 for 15.8 wt %.

The calcined material is modified by the alkaline ion exchange method. The procedure consisted of suspending the SnHYDx material in an aqueous solution of KCl (0.5 M, 100 mL g^{-1} of zeolite) with stirring (120–150 rpm) for 2 h at room temperature. The final catalyst (KSnHYDx) was filtered, dried at 105 °C overnight, and calcined with the same previous step calcination procedure.

2.3. Catalysts characterization

The prepared metal-modified zeolite Y-based catalysts were characterized by employing several characterization techniques. The textural properties were determined by nitrogen physisorption using a Micromeritics 3Flex-3500 at −196 °C using 50–100 mg of the catalysts. First, the sample was degassed ex-situ in a Micromeritics VacPrep 061 Sample Degas System under vacuum at 180 °C overnight, followed by in-situ degassing in the physisorption equipment under vacuum for 4 h at 250 °C. The specific surface area was calculated using the BET and Dubinin-Radushkevich methods and the pore size, pore volume, and pore size distribution were calculated with the Horvath-Kawazoe and the non-local density functional theory (N_2-Tarazona NLDFT) methods.

The phase purity and identification of the crystal phases were determined by powder X-ray diffraction (XRD), whose patterns were recorded using a PANalytical Empyrean diffractometer with five axis goniometers. The incident beam optics consisted of Bragg-Brentano HD x-ray mirror, fixed 1/4° divergence slit, 10 mm mask, 0.04 rad soller slit and 1° antiscatter slit. The diffracted beam optics consisted of 7.5 mm divergence slit, 0.04 rad soller slit and PIXcel detector array. The used x-ray tube was Empyrean Cu LFF. The X-ray radiation was filtered to include only $CuK_{\alpha 1}$ and $CuK_{\alpha 2}$ components. The results were analyzed with MAUD (Material Analysis Using Diffraction) analysis program [70]. Instrumental broadening was evaluated with Si standard sample. The results were obtained with 2θ scan range from 5° to 120°.

The strength and concentrations of both Brønsted and Lewis acid sites were measured using Fourier Transform Infrared Spectroscopy (FTIR) and pyridine as the probe molecule. Pyridine-FTIR spectra were acquired with an IRTracer-100 (Shimadzu) spectrophotometer pressing the solid catalysts into thin wafers and placed into the FTIR cell, which was outgassed and heated to 450 °C for 1 h. After that, the cell was cooled to 100 °C and the background spectrum was recorded. Pyridine (> 99 wt %, Acros Organics) was adsorbed on the solid surface for 30 min followed by measurements after desorption at 250 °C, 350 °C, and 450 °C under vacuum for 1 h at each temperature. Brønsted acid sites (BAS) and Lewis acid sites (LAS) were identified using the spectral bands at 1545 cm^{-1} and 1450 cm^{-1}, respectively, and the corresponding concentrations were calculated using the extinction coefficients reported by Emeis [71].

The catalyst morphology was investigated by transmission electron microscopy (TEM) with a JEM-1400Plus (JEOL, Japan) instrument. Prior to analysis, the catalyst samples were suspended in ethanol and affixed to a copper grid. To determine the average size of metal particles, the diameter of more than 200 particles was measured using ImageJ software. Additionally, the crystal morphology of the catalysts was examined through scanning electron microscopy (SEM) using a Zeiss Leo Gemini 1530 instrument, which was equipped with a Thermo Scientific UltraDry Silicon Drift Detector (SDD).

The total acidity strength was measured using NH_3-Temperature Programmed Desorption (NH_3-TPD) on a BELCAT II analyzer (Microtrac MRB). Initially, approximately 50 mg of the sample underwent in-situ activation at 500 °C for 1 h (ramping at 10 °C min^{-1}). Subsequently, the sample was cooled to 50 °C under a helium flow (30 mL min^{-1}) and saturated with a gas mixture of 5 vol % NH_3/He (30 mL min^{-1}) for 1 h. Physisorbed ammonia was then flushed with helium (30 mL min^{-1}) at 50 °C for 1 h. Finally, the sample underwent heating to 600 °C at a rate of 10 °C min^{-1} under a helium flow of 30 mL min^{-1} for the desorption of NH_3.

Basicity was measured using CO_2-Temperature Programmed Desorption (CO_2-TPD), which was carried out on a BELCAT II analyzer (Microtrac MRB). First, around 50 mg of sample was activated in-situ at 500 °C for 2 h (10 °C min^{-1}). Then, the sample was cooled down at 50 °C while flowing helium (30 mL min^{-1}) and saturated with 30 mL min^{-1} of a gas mixture of 5 vol % CO_2/He for 1 h. Physisorbed CO_2 was flushed with 30 mL min^{-1} He at 50 °C for 1 h. Finally, the sample was heated up to 900 °C with a heating rate of 10 °C min^{-1} under a helium flow of 30 mL min^{-1} for the desorption of CO_2.

UV–Vis reflectance spectra were obtained using an Avantes Avaspec HS-TEC CCD spectrometer, coupled with an Avantes FC-UV600-1-SR fiber optic cable of 600 μm diameter. The light source employed was the Avantes Ava-Light-DHc, which utilized deuterium and halogen lamps. A $BaSO_4$ disc from Edinburgh Instruments served as the reference.

The ^{29}Si and ^{27}Al MAS NMR spectra were recorded on a Bruker AVANCE-III spectrometer operating at 79.50 MHz (^{29}Si) and 104.26 MHz (^{27}Al) using a CP-MAS 4 mm solid state probe. The ^{27}Al spectra were obtained with a 90° pulse (zg0) and a recycle delay of 0.05 s at a spinning speed of 14 kHz, while the ^{29}Si spectra were acquired with a 90° pulse (zg) and a recycle delay of 100 s at a spinning speed of 14 kHz.

The characterization of the spent catalyst also included powerful techniques to detect and quantify the coke formation such as temperature-programmed oxidation (O_2-TPO)-mass spectrometry (MS) and thermogravimetric (TGA) analysis. O_2-TPO was carried out on a BELCAT II analyzer (Microtrac MRB) coupled with a mass spectrometer (Pfeiffer OmniStar GSD 350). First, around 200 mg of the sample was pre-treated at 120 °C for 2 h (10 °C min^{-1}), followed by cooling to 35 °C. The analysis was carried out by heating up to 900 °C at 5 °C min^{-1} using a 30 mL min^{-1} of a mixture of 5 vol% O_2/Ar. The holding time of the target temperature was 10 min. TGA was performed using an SDT650 TA Instrument equipped with a 90 μL alumina sample cup. About 5 mg of the samples were heated in an air flow of 100 mL min^{-1} from room temperature up to 800 °C at 10 °C min^{-1} and held for 6 s. The results obtained for the spent catalyst were compared to the results for the fresh one.

2.4. Catalytic tests

The epoxidation reaction of R-(+)-limonene with H_2O_2 as the oxidizing agent was carried out in the liquid phase using a 100 mL three-neck glass flask as a batch reactor. The flask was equipped with a thermocouple, a sampling valve, and a condenser that utilized glycol as the coolant fluid (at 1 °C). The setup also included an oil-heating jacket (ECO E4 Silver immersion thermostat) and mechanical stirring (Heidolph RZR-2041 instrument) for precise temperature control and mixing. In a typical experiment, 1.9611 g (14.40 mmol) of limonene and 43 mL of the solvent were loaded into the reactor. The solution was then preheated to a reaction temperature of 70 °C while stirring at 750–800 rpm. Next, 2.4483 g (71.98 mmol) of H_2O_2 was added to the reactor. After a few minutes, when the reactor temperature stabilized, the catalyst (648 mg) was rapidly introduced, marking the start time of the reaction. Approximately 0.6 mL samples were taken at specific time intervals and analyzed using a Shimadzu Nexis GC-2030 equipment equipped with a DB-225 capillary (30 m length x 320 μm internal diameter x 0.25 μm film thickness), an FID detector, and an autosampler. Helium was used as the carrier gas (24 mL min^{-1}) with a split ratio of 10:1. The detector temperature was set to 250 °C, and the injection volume was 1 μL. The oven-temperature program ramped from 50 °C to 220 °C at a rate of 10 °C min^{-1} and was held for 1 min. The nature of the products was further confirmed with an Agilent GC/MS 6890 N/5973 N equipped with a DB-1 capillary column (30 m length x 250 μm internal diameter x 0.5 μm film thickness).

The R-(+)-limonene conversion (X_L), the selectivity to the product i (S_i), and the yield to the product (Y_i) were calculated based on Eqs. (1)–(3).

$$X_L(\%) = \frac{n_{L,0} - n_{L,t}}{n_{L,0}} * 100 \tag{1}$$

$$S_i(\%) = \frac{n_{i,t}}{n_{L,0} - n_{L,t}} * 100 \tag{2}$$

$$Y_i(\%) = \frac{n_{i,t}}{n_{L,0}} * 100 = \frac{X_L * S_i}{100} \tag{3}$$

Where $n_{L,0}$, $n_{L,t}$, and $n_{i,t}$ represent the initial moles of limonene, the moles of limonene after a time t, and the moles of the product i after a time t, in the reaction mixture, respectively. The concentrations of limonene as the substrate and different oxidation products such as cis (−)-1,2-epoxide, trans (−)-1,2-epoxide, (4R, 8RS)-limonene-8,9-epoxide, dihydrocarvone, carveol, carvone, limonene diepoxide, and limonene diol were determined from the multipoint calibration curves.

The initial reaction rate ($-r_{L,0}$) and turnover frequency (TOF) for limonene can be calculated using Eqs. (4) and (5), where $C_{L,0}$ corresponds to the initial molar concentration of limonene, V is the total reaction volume, X is the conversion, m is the catalyst mass, Δt is the time interval (2 h), and TA is the total acidity measured by pyridine-FTIR.

$$-r_{L,0} = \frac{C_{L,0} * V * X}{m * \Delta t} \tag{4}$$

$$TOF = \frac{-r_{L,0}}{TA} \tag{5}$$

For the reusability test, the catalyst was recovered from the reaction mixture through filtration, followed by abundant washing with acetone. Subsequently, the solid was dried at 105 °C overnight. This resulting solid was labeled as “spent”. Leaching tests were conducted using the

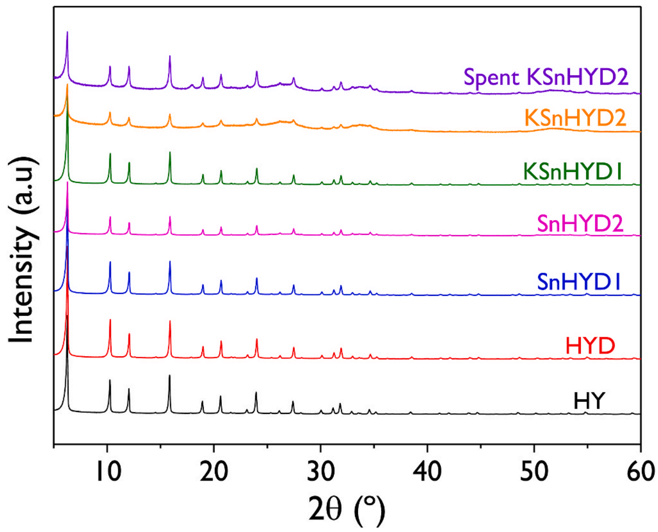

Fig. 2. XRD patterns of the catalysts.

hot-filtration method to remove the catalyst from the reaction mixture. The reaction proceeded for 4 h, after which the catalyst was separated from the liquid at the reaction temperature. A liquid aliquot was then analyzed by GC to quantify limonene conversion and product selectivity, while the remaining mixture continued to react for an additional 20 h. Finally, the sample was analyzed by GC to determine the conversion after removing the catalyst.

2.5. Quantification of H_2O_2

The H_2O_2 concentration was followed in the reaction via titration using a cerium sulfate solution as has been reported in the literature [72]. An aliquot of the reaction sample was accurately weighed and placed in an Erlenmeyer flask containing 50 mL of H_2SO_4 (10 % w/v) and sufficient amount of ice to maintain the temperature between 0 and 10 °C. Two drops of the ferroin indicator were added and the flask solution was titrated with 0.1 N ammonium cerium (IV) sulfate solution until the disappearance of the salmon color by formation of a light blue. The H_2O_2 concentration ($C_{H_2O_2}$) and conversion ($X_{H_2O_2}$) can be calculated according to Eqs. (6) and (7), respectively.

$$C_{H_2O_2}(\text{wt. \%}) = \frac{V_T C_T MW_{H_2O_2}}{\theta_{SF} W_s} * 100 \tag{6}$$

$$X_{H_2O_2} = \frac{C_{H_2O_2,0} - C_{H_2O_2}}{C_{H_2O_2,0}} \tag{7}$$

Where θ_{SF} refers to the stoichiometric factor of $(NH_4)_4Ce(SO_4)_4$:H_2O_2 with a value of 2, C_T is the concentration of the titrant (0.1 mol L^{-1}), V_T is the volume of the spent titrant, $MW_{H_2O_2}$ is the molecular weight of H_2O_2 (34.01 g mol^{-1}), W_s is the sample weight, and $C_{H_2O_2,0}$ is the H_2O_2 initial concentration.

3. Results and discussion

3.1. Catalyst characterization

3.1.1. X-ray diffraction (XRD) patterns

The XRD patterns for the prepared catalysts are illustrated in Fig. 2. All diffraction patterns can be adequately explained by the presence of faujasite (ICSD 24869) and SnO (ICSD 92552) phases. In all samples, ordered structures are evident, as indicated by the narrow diffraction peaks corresponding to the main crystallographic planes (111), (220), (311), (331), (511), (440), (533), (642), and (555) located at 2θ = 6.2°, 10.1°, 11.9°, 15.6°, 18.6°, 20.3°, 23.6°, 26.9°, and 31.3°, respectively [73,74]. The ordered structures are clearly visible in all samples, as shown in Figs. S1–S7.

Concerning the Sn species, some broad diffraction peaks are observed at 33°, associated with the SnO phase [75], and at 26.5° and 51.7°, associated with SnO_2 [76], in SnHYD2, KSnHYD2, and spent KSnHYD2 materials (Figures S4, S6 and S7). Although the refinement of the diffraction models suggests minor SnO traces in the SnHYD1 and KSnHYD1 catalysts (Figs. S3 and S5), their identification from the XRD

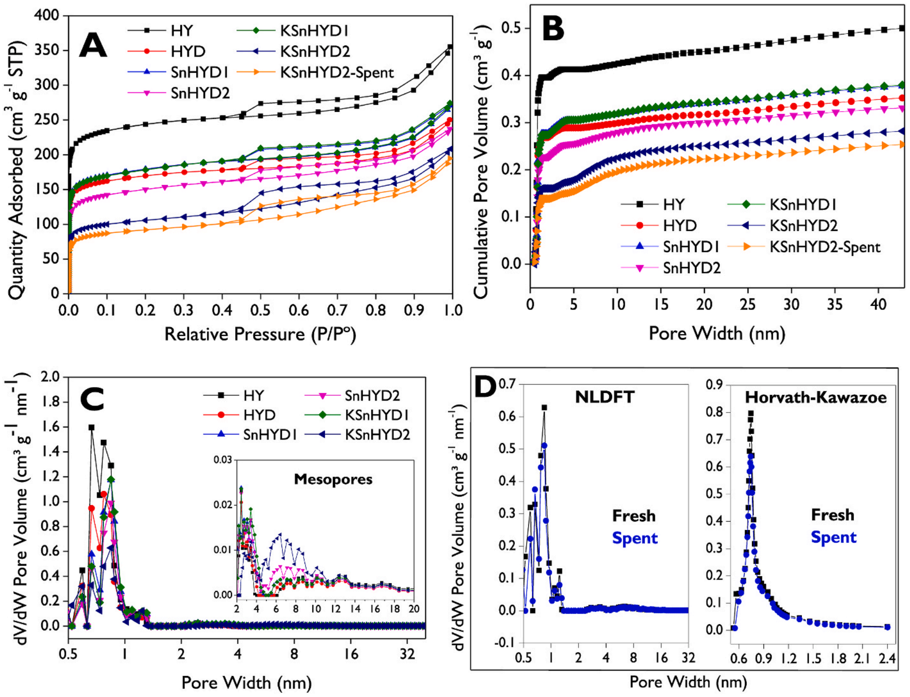

Fig. 3. N_2 adsorption-desorption isotherms **(A)**, cumulative pore volume **(B)**, pore size distribution of the fresh materials **(C)**, and pore size distribution of the fresh and spent KSnHYD2 **(D)**.

Table 2
Textural properties of the prepared catalysts.

Catalyst	SA_{BET} (m^2 g^{-1})	$SA_{Dubinin}$ (m^2 g^{-1})	APS^b (Å)	V_{mic} (cm^3 g^{-1})	V_{mes} (cm^3 g^{-1})	V_T (cm^3 g^{-1})	$Mesoporosity^c$ (%)	V_{mic}/V_{mes}
HY	789	1115	6.6	0.40	0.10	0.50	20	3.8
HYD	553	753	7.7	0.27	0.08	0.35	23	3.2
SnHYD1	586	816	8.4	0.28	0.10	0.38	26	2.7
KSnHYD1	584	809	8.5	0.27	0.11	0.38	28	2.6
SnHYD2	493	674	8.4	0.23	0.10	0.33	31	2.2
KSnHYD2	348	465	8.5 (7.5)	0.16	0.12	0.28	43	1.3
KSnHYD2S[a]	302	407	8.5 (7.5)	0.14	0.12	0.26	45	1.2

SA: surface area. **APS:** Average pore size estimated from the pore size distribution with the NLDFT method (Fig. 3). $\mathbf{V_{mic}}$**:** Micropores volume. $\mathbf{V_{mes}}$**:** Mesopores volume. $\mathbf{V_T}$**:** Total pore volume. [a] S denotes spent catalyst. [b] Value in parenthesis was estimated by Horvath-Kawazoe method. [c] Mesoporosity is calculated as the V_{mes}/V_T ratio.

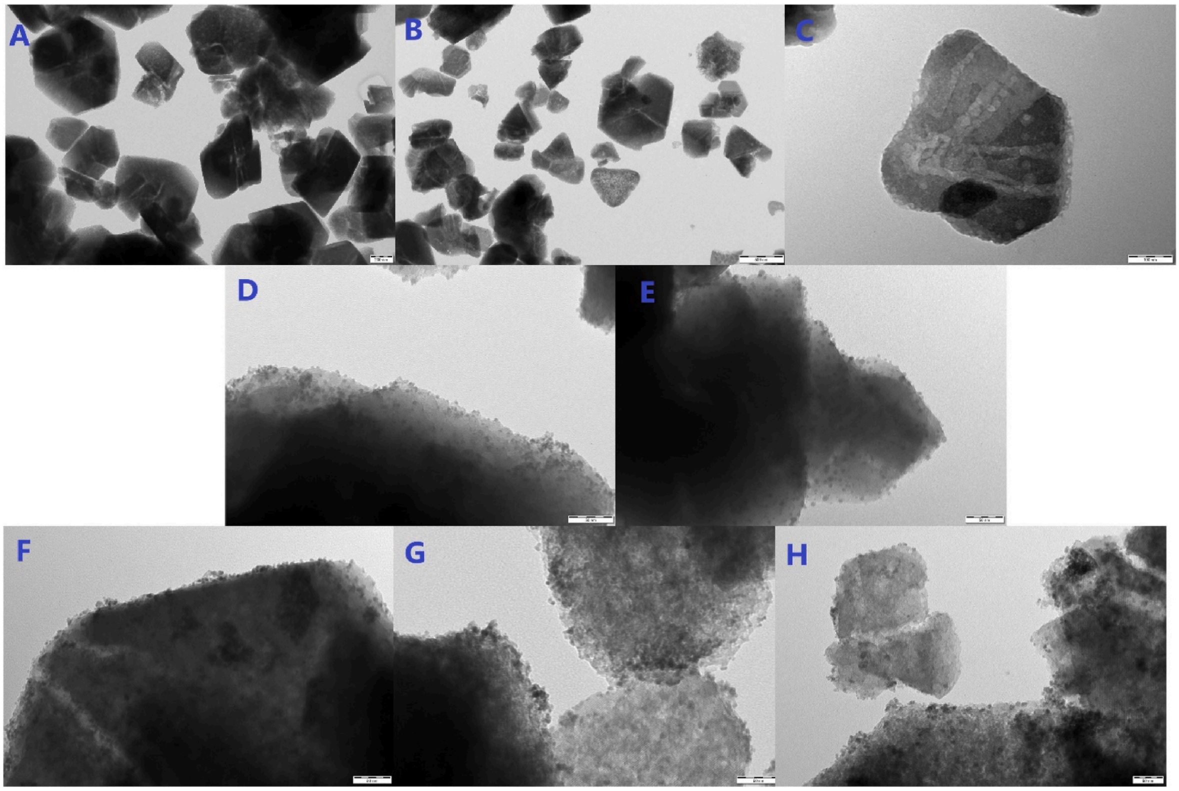

Fig. 4. TEM images of **(A)** HY, **(B)** HYD (×12000), **(C)** HYD (×60000), **(D)** SnHYD1, **(E)** KSnHYD1, **(F)** SnHYD2, **(G)** KSnHYD2, **(H)** KSnHYD2-Spent. The ruler sizes for the images are 50 nm (**D, E, F, G, H**), 100 nm (**C**), 200 nm (**A**), and 500 nm (**B**).

patterns is more speculative.

3.1.2. Textural properties

The textural properties of the catalytic materials were measured using N_2 adsorption-desorption isotherms and are illustrated in Fig. 3 and Table 2. The presence of mesopores in all materials, including the parent zeolite (HY), is confirmed by Fig. 3A, whose isotherms exhibited type IV hysteresis associated with the capillary condensation that occurs inside the pores [77]. The plots of the cumulative pore volumes as a function of the pore width (Fig. 3B) increase more rapidly in the microporosity range than the mesoporosity range for all the materials, indicating that the volume of micropores is larger than the volume of mesopores ($V_{mic}/V_{mes} > 1$), as displayed in Table 2. The pore size distributions (Fig. 3C) illustrate average pore sizes (APS) for the catalysts ranging from 6.6 to 8.5 Å (Table 2), with the lowest values for the parent (HY) and dealuminated (HYD) zeolites. The catalysts modified with Sn and/or K did not exhibit appreciable differences regarding the metals loading. Therefore, the results suggest that the post-incorporation of Sn (either 2% or 15.8% nominal loading) to the dealuminated zeolite as the support led to an increase in the APS of materials, although modification of tin-modified zeolites with K by the alkaline ion exchange method did not lead to any dependence on the pore size since the values were similar (8.4–8.5 Å). It is worth mentioning, according to Fig. 3D, that spent KSnHYD2 did not exhibit any change in the APS compared to the fresh one, even with two methods such as NLDFT and Horvath-Kawazoe, yielding values of 8.5 and 7.5 Å, respectively.

On the other hand, the specific surface areas, reported in Table 2, were calculated by the conventional Brunauer-Emmett-Teller (BET) method but also with a powerful method deduced from the micropore filling theory like the Dubinin-Radushkevich method [78], perfectly applicable for these hierarchical zeolites Y-based catalysts. The first observation is that the Dubinin areas are ca. 34–41% larger than BET areas. The parent zeolite (HY) exhibited the highest surface area of about 1115 m^2 g^{-1}, while the dealuminated zeolite (HYD) possessed a specific area of around 753 m^2 g^{-1}, resulting from a successful nitric acid treatment forming mesopores in the zeolitic structures. Incorporation of 2% Sn nominal loading (SnHYD1) and K (KSnHYD1) did not exhibit appreciable changes in the surface areas, with values ranging from 753 to 816 m^2 g^{-1}, while a higher Sn loading (nominal 15.8%) showed a decrease in the surface area of around 10% (SnHYD2) compared to the

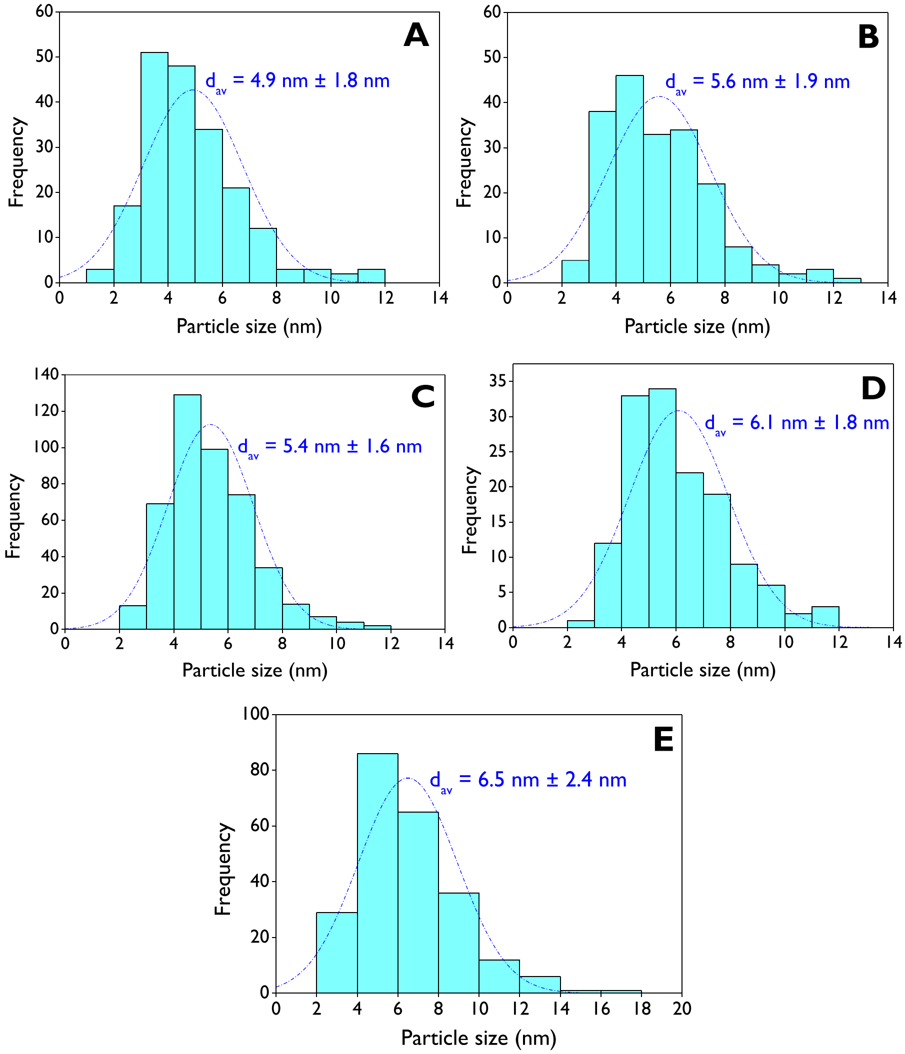

Fig. 5. Particle size distribution of **(A)** SnHYD1, **(B)** SnHYD2, **(C)** KSnHYD1, **(D)** KSnHYD2, **(E)** KSnHYD2-Spent.

dealuminated support, explained by possible pore blocking or clogging. When this tin-modified zeolite was further modified with K (KSnHYD2), an appreciable decrease in the area was observed, around 31% (465 m^2 g^{-1}), suggesting that potassium incorporation into the tin-modified zeolites can tune the total surface area. On the other hand, the surface area for spent KSnHYD2 showed a decrease concerning the fresh one of around 13% (407 m^2 g^{-1}). The mesoporosity, calculated as the ratio between the mesoporous and total volumes, is shown in Table 2, indicating the lowest value (20%) for the parent zeolite (HY) and the higher values for KSnHYD2 (43%). It is worth noticing that mesoporosity did not change significantly after their use in the reaction (45%).

3.1.3. *Transmission electron microscopy (TEM)*

The TEM images for the fresh catalysts and the spent KSnHYD2 are shown in Fig. 4 and Figs. S8–S14. Micrographs of the dealuminated zeolite (Fig. 4B and 4C) exhibited large cavities, clearly indicating the successful creation of mesopores in the structure, at the same time the nitric acid treatment did not cause a collapse in the structure. Additionally, the parent zeolite also exhibited some cavities (Fig. 4A) corresponding to mesopores but in a lesser extent than the dealuminated one, which was confirmed by the N_2 physisorption results (Table 2) with 20% of mesoporosity for that material. On the other hand, TEM images for Sn-modified zeolites (Fig. 4D and 4F) and K–Sn-modified zeolites (Fig. 4E and 4G) show well-dispersed metal particles over the support. Despite the previous qualitative information obtained from the TEM analysis, the distribution of metal particle sizes (Fig. 5) can be plotted from at least 200 measurements for each catalyst image. All fresh metal catalysts exhibited an average particle size ranging from 4.9 nm to 6.1 nm, indicating a direct relationship between the tin loading and the particle size, as the lowest values were obtained for the catalysts with the lower tin loading (SnHYD1 and KSnHYD1,Fig. 5A and 5C) and the highest values for the higher tin loading (SnHYD2 and KSnHYD2, Fig. 5B and 5D). Notice that the obtained distributions are unimodal, indicating that it is not possible to discern the average particle size for K and Sn individually from the TEM images due to their similar sizes.

3.1.4. *Scanning electron microscopy – energy dispersive X-rays (SEM-EDX)*

The SEM micrographs of the synthesized catalysts are presented in Fig. 6. All materials exhibit various crystal shapes such as pyramidal, rectangular, hexagonal, triangular, and agglomerates with crystal sizes ranging from 100 to 600 nm (Figs. S15–S21). However, the materials do not show a visibly uniform distribution of the metal particles over the dealuminated support. This could be attributed to the use of $SnCl_4·5H_2O$ as the precursor, as observed recently in our group. The most important observation from the SEM images is that the dealumination procedure of the HY zeolite was successful, as evidenced by the absence of the structure collapse. Conversely, larger particles were broken to create more mesoporosity (Table 2).

On the other hand, the elemental composition was determined by EDX and is reported in Table 3 in weight percentage for both atomic and

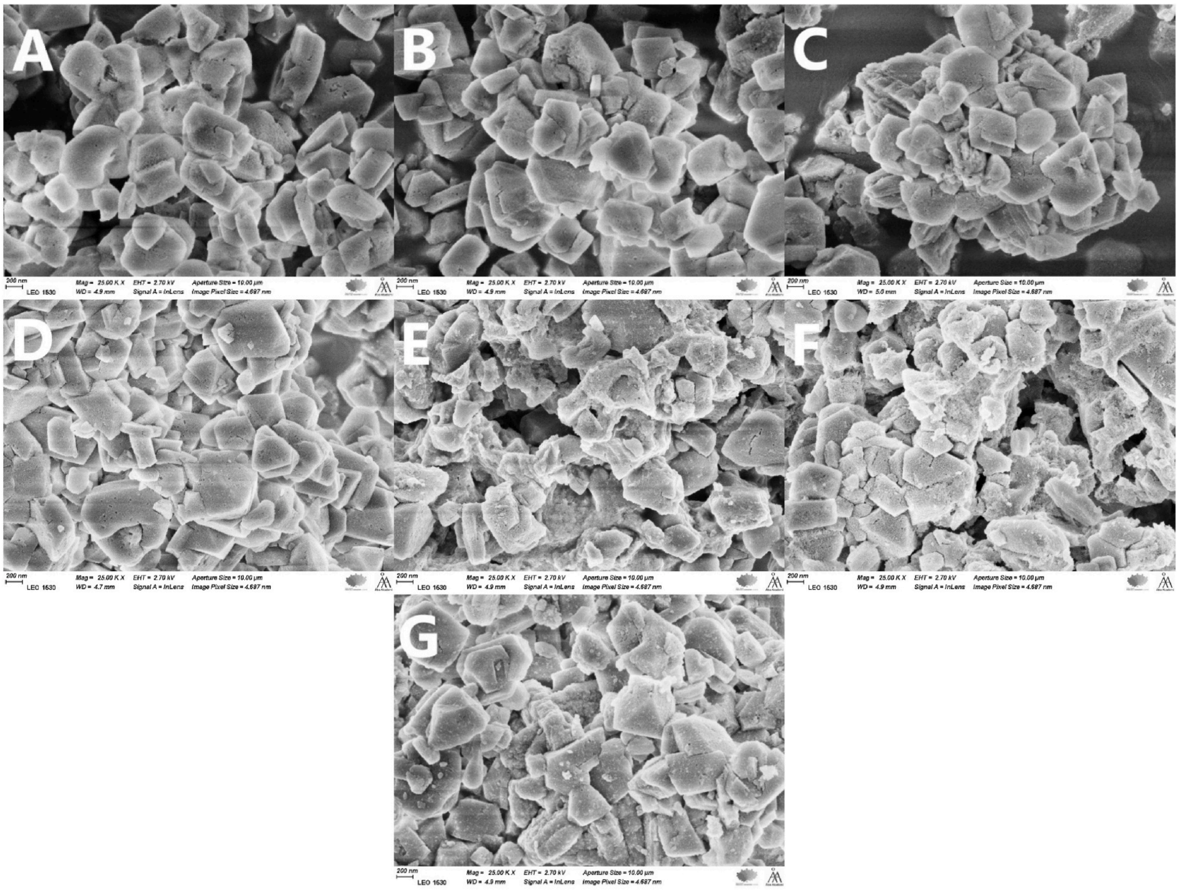

Fig. 6. SEM images of **(A)** HY, **(B)** HYD, **(C)** SnHYD1, **(D)** KSnHYD1, **(E)** SnHYD2, **(F)** KSnHYD2, **(G)** KSnHYD2-Spent.

Table 3
Elemental composition of the materials using SEM-EDX analysis.

Catalyst	Weight %									SiO_2/Al_2O_3 mole ratio
	SiO_2	Al_2O_3	SnO_2	K_2O	Si	Al	O	Sn	K	
HY	94.29	5.71	0.00	0.00	44.07	3.02	52.90	0.00	0.00	28.0
HYD	97.74	2.26	0.00	0.00	45.69	1.19	53.12	0.00	0.00	73.4
SnHYD1	94.96	1.68	3.37	0.00	44.39	0.89	52.07	2.65	0.00	95.9
KSnHYD1	93.56	2.90	3.04	0.51	43.73	1.53	51.92	2.39	0.42	54.8
SnHYD2	78.53	2.32	19.14	0.00	36.71	1.23	46.98	15.08	0.00	57.4
KSnHYD2[a]	78.28	1.98	16.54	2.66	36.59	1.05	46.58	13.02	2.21	67.09

[a] The balance (0.55) corresponds to Cl.

Table 4
Acidity of the catalysts by FTIR using pyridine as probe molecule.

Catalyst	Brønsted acidity (µmol g^{-1})				Lewis acidity (µmol g^{-1})				BA/LA ratio	Total (µmol g^{-1})
	Weak	Medium	Strong	Total	Weak	Medium	Strong	Total		
HY	10	20	190	220	19	10	26	55	4.0	275
HYD	17	2	10	29	19	2	6	27	1.1	56
SnHYD1	9	8	9	26	21	5	10	36	0.7	62
KSnHYD1	3	6	6	15	12	6	7	25	0.6	40
SnHYD2	10	3	6	19	38	14	10	62	0.3	81
KSnHYD2	1	0	3	4	20	2	6	28	0.1	32
KSnHYD2S[a]	2	1	1	4	14	9	3	26	0.2	30

[a] S denotes spent catalyst.

oxides. As the parent zeolite (HY) was investigated without further treatment, the SiO_2/Al_2O_3 molar ratio of ca. 28.0 was expected, given the nominal SiO_2/Al_2O_3 ratio of 30. The dealuminated zeolite (HYD) and metal-modified catalysts showed that this ratio was larger than 28.0, easily explained by creation of mesopores resulting from the removal of aluminum from the starting zeolite. The nominal Sn loading can be compared with the experimental values obtained by EDX, resulting in 2.65% and 2.39% of Sn for SnHYD1 and KSnHYD1,

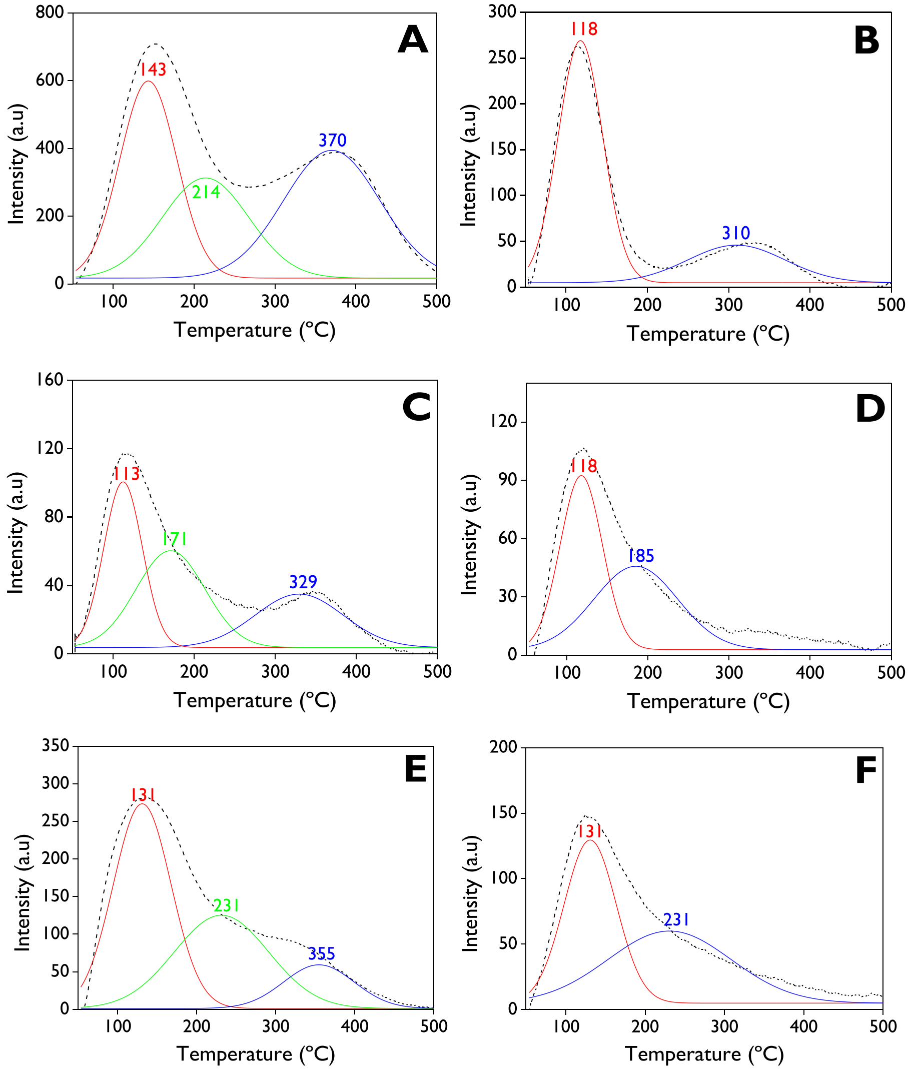

Fig. 7. NH_3-TPD profiles for the fresh catalysts: **(A)** HY, **(B)** HYD, **(C)** SnHYD1, **(D)** KSnHYD1, **(E)** SnHYD2, **(F)** KSnHYD2.

Table 5
Acidity of the catalysts by NH_3-TPD.

Catalyst	Acidity (mmol g^{-1})			
	Weak	Medium	Strong	Total
HY	64	45	53	162
HYD	23	0	11	34
SnHYD1	6	6	4	16
KSnHYD1	7	7	0	14
SnHYD2	32	14	11	57
KSnHYD2	12	11	0	23

respectively, while obtaining 15.08% and 13.02% for SnHYD2 and KSnHYD2, respectively. The K loadings presented a maximum of 2.21% for KSnHYD2.

3.1.5. Catalysts acidity and basicity

The quantification of Brønsted (BA) and Lewis (LA) acid sites (Table 4, Fig. S22) in the catalytic materials was performed using pyridine as a probe molecule in the adsorption-desorption FTIR analysis. The parent zeolite (HY) exhibited the highest total acidity (275 μmol g^{-1}) and the highest BA/LA ratio (4.0), associated with the highest aluminum amount (Table 3). After dealumination, the materials showed significantly lower Brønsted acidity reflected in both total acidity and

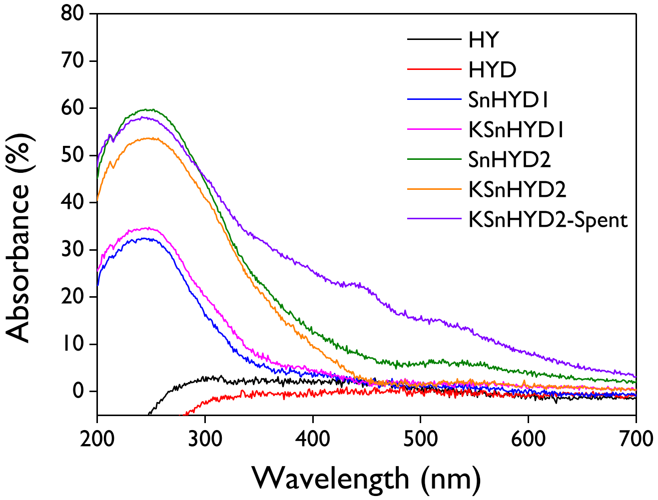

Fig. 8. UV–Vis-DRS spectra of the catalysts.

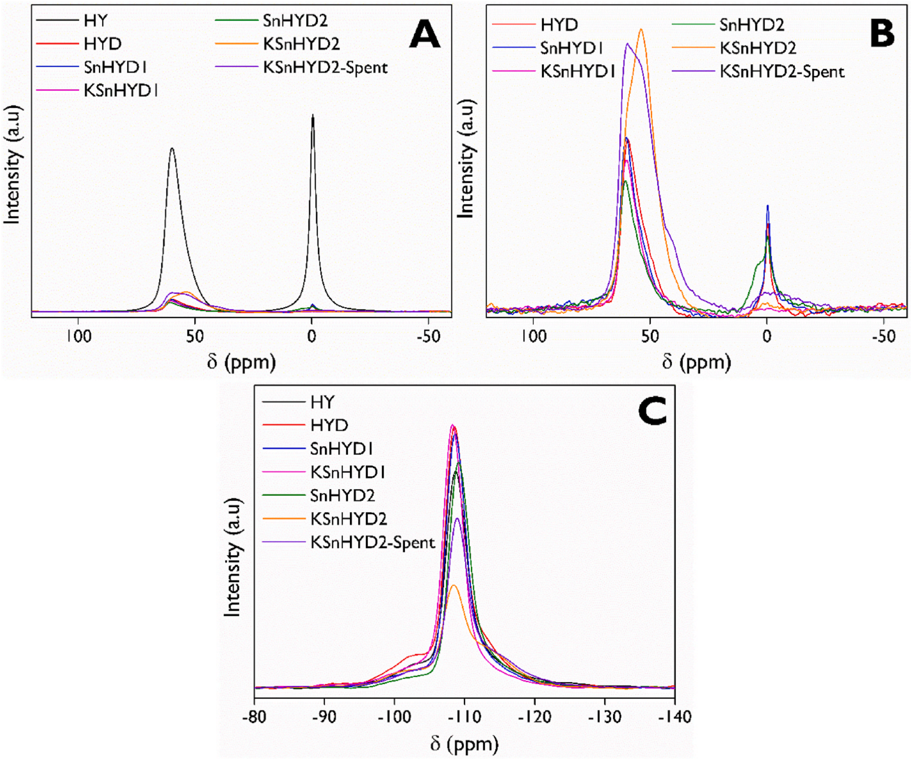

Fig. 9. **(A, B)** ^{27}Al MAS NMR and **(C)** ^{29}Si MAS NMR spectra of catalysts.

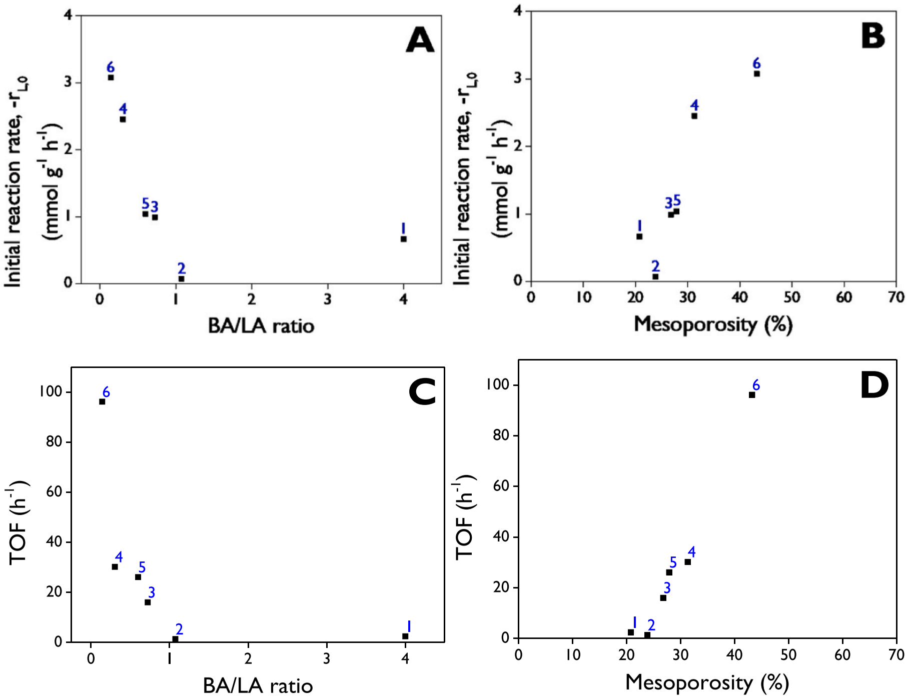

Fig. 10. Initial reaction rate (A, B) and turnover frequency (C, D) as functions of Brønsted (BA)/Lewis (LA) acidity ratio and mesoporosity fraction. (1) HY, (2) HYD, (3) SnHYD1, (4) SnHYD2, (5) KSnHYD1, (6) KSnHYD2.

the BA/LA ratios. When Sn was anchored on the dealuminated zeolite, an increase in total acidity was observed, primarily associated with an increase in Lewis acidity, resulting in values of 62 and 81 μmol g^{-1} for SnHYD1 and SnHYD2, respectively. The difference between them can be explained by variations in the loading of Sn onto the catalysts (2.65% and 15.08%, respectively, Table 3). On the other hand, incorporation of K into the catalysts led to a decrease in total acidity and the BA/LA ratio, mainly associated with lower Brønsted acidity. The spent KSnHYD2 exhibited acidity values similar to the fresh one. The lowest BA/LA ratios were obtained with the highest tin loadings (SnHYD2 and KSnHYD2).

The acidity strength of the catalysts was also studied by NH_3-TPD,

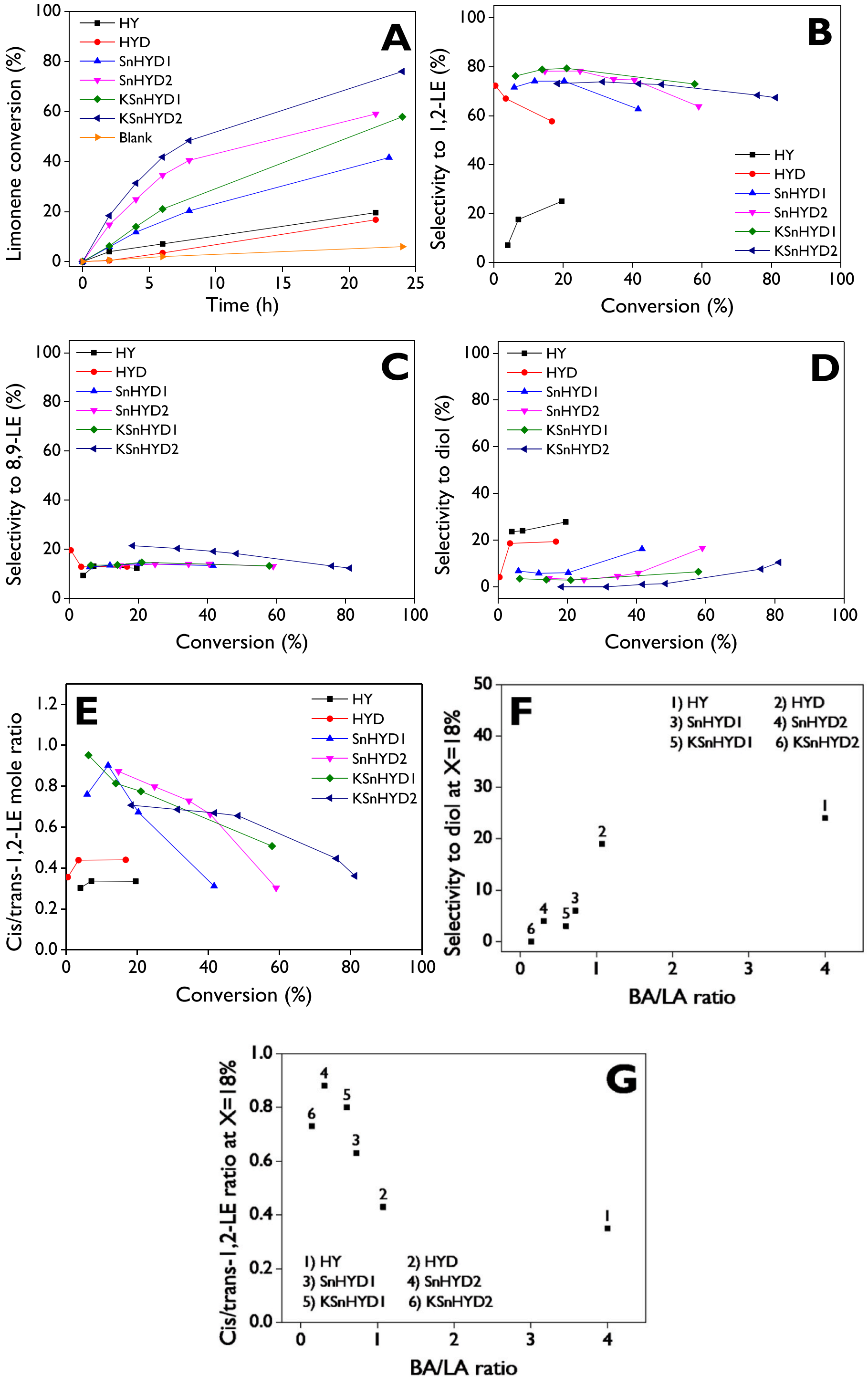

Fig. 11. Role of catalyst in the R-(+)-limonene conversion and product distribution: Limonene conversion as a function of the reaction time **(A)**; selectivity to limonene-1,2-epoxides **(B)**, selectivity to limonene-8,9-epoxides **(C)**, selectivity to limonene diol **(D),** and *cis/trans*-limonene-1,2-epoxide molar ratio **(E)** as a function of the conversion; selectivity to diol **(F)** and *cis/trans*-1,2-LE molar ratio **(G)** at 18% conversion as a function of the BA/LA ratio. **Reaction conditions:** $C_{L,0} = 0.27$ M, acetonitrile as a solvent, H_2O_2/limonene molar ratio = 5:1, 432 mg of catalyst, 70 °C, 800 rpm.

quantified according with Eq. (8) [79,80], where n_{Des} are the desorbed moles of ammonia, $\dot{V}_{He}$ is the volumetric flow of carrier gas, V_m is the molar volume of 1 mol of ideal gas at standard conditions (22.4 L mol^{-1}), β is the heating rate and C_i is the ammonia concentration (% vol).

$$n_{Des} = \frac{\dot{V}_{He}}{V_m}\frac{1}{\beta}\int_{T_0}^{T_f} C_i dT \tag{8}$$

The acidity strength is classified as weak, medium, and strong acidity, related with the bands of the deconvoluted TCD signal in the different temperatures ranges of <150 °C, <250 °C, and >250 °C, as is shown in Fig. 7. Parent zeolite (HY) and tin-dealuminated zeolites (SnHYD1 and SnHYD2) exhibited weak, medium, and strong acid sites, while potassium-modified catalysts showed the absence of strong acidity due to the lack of a band at high temperature. Table 5 shows the acidity strength values measured by NH_3-TPD, observing a close relationship

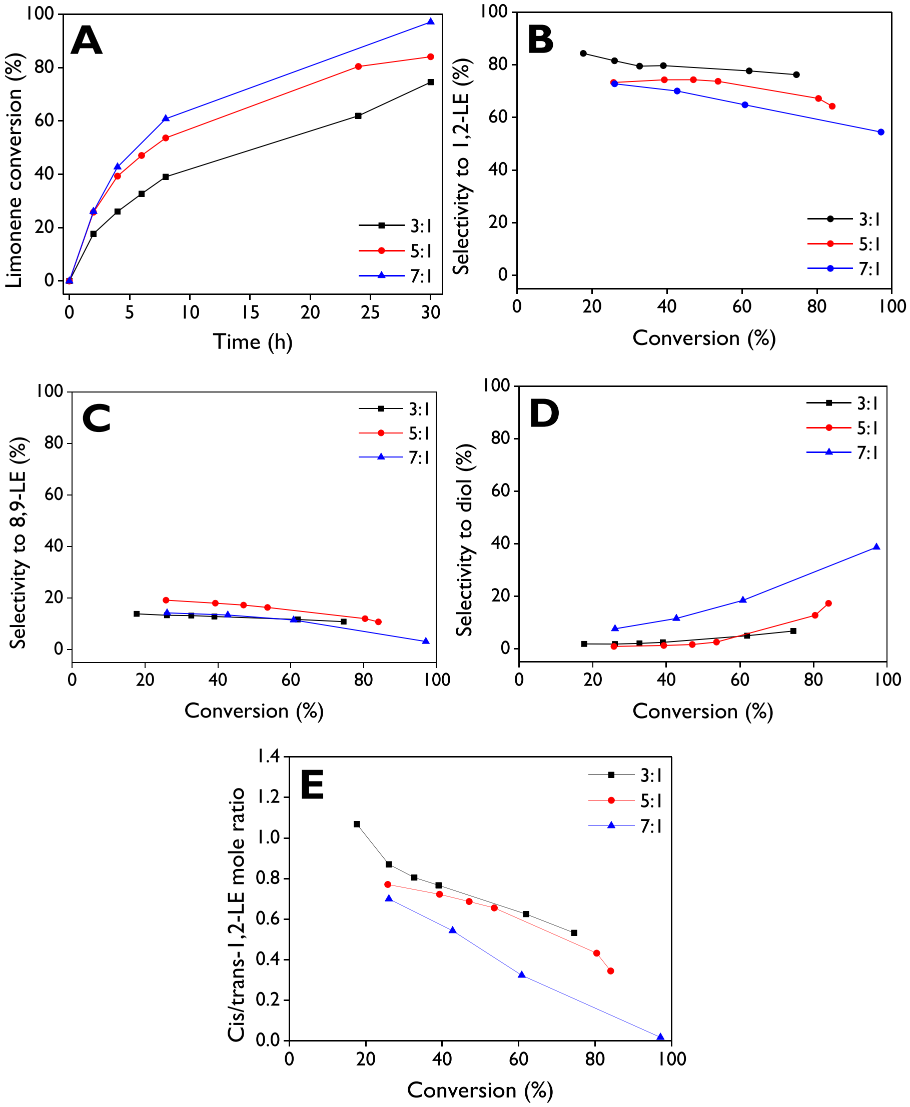

Fig. 12. Effect of the H_2O_2/limonene molar ratio in the R-(+)-limonene conversion and product distribution over KSnHYD2 as a catalyst: Limonene conversion as a function of the reaction time **(A)**; selectivity to limonene-1,2-epoxides **(B)**, selectivity to limonene-8,9-epoxides **(C)**, selectivity to limonene diol **(D)**, and *cis/trans*-limonene-1,2-epoxide molar ratio **(E)** as a function of the conversion. **Reaction conditions:** $C_{L,0} = 0.27$ M, acetonitrile as a solvent, 648 mg of catalyst, 70 °C, 800 rpm.

between these results with the pyridine-FTIR (Fig. S23).

Basicity of the potassium-modified catalysts was investigated using CO_2-TPD analysis coupled with mass spectrometry. Results showed absence of basic sites as no signal was observed in desorption of CO_2, as shown in Fig. S24. Furthermore, these results were expected according to the EDX analysis (Table 3).

3.1.6. UV–vis-DRS analysis

The UV–Vis-DRS analysis (Fig. 8) is one of the most widely used methods for assessing the environment of the metal Lewis-acid center in zeolites [81]. The peak at ca. 210 nm observed in materials with the highest Sn loading (SnHYD2, KSnHYD2, and spent KSnHYD2) is attributed to the absorption of isolated Sn^{4+} species in tetrahedral coordination located inside the channels of the mesopores of hierarchical zeolites [82]. The wide band observed between 200 and 300 nm for all materials has been assigned to extra-framework Sn species, namely octahedrally coordinated and/or oligomeric Sn species [81,83,84], which could be present in synthesized catalysts with Sn (IV) centers located outside the zeolite pores [79,85]. Spectra for the parent (HY) and dealuminated (HYD) zeolites exhibited no bands, as expected. On the other hand, the spent KSnHYD2 showed a shoulder around 450 nm, which can be associated with impurities after the reaction.

3.1.7. Solid-state NMR

This technique has been established as an efficient method to determine the coordination and local structure of Si and Al species in zeolites [86]. Fig. 9 illustrates the ^{27}Al spectra (Fig. 9A and 9B) and the ^{29}Si spectrum (Fig. 9C) for all synthesized catalysts. Two well-defined ^{27}Al resonances around 60 and 0 ppm are observed for all the samples, attributed to the four-coordinated framework Al and six-coordinated extra-framework Al, respectively [86,87], although some authors have recently assigned the resonance at 0 ppm to aluminum entities with octahedral coordination [88]. The absence of resonance around 30 ppm indicates the absence of five-coordinated extra-framework Al [89]. Specifically, materials with potassium displayed a slight resonance at 0 ppm, as shown clearly in Fig. 9B. On the other hand, the resonance observed around −110 ppm for ^{29}Si NMR (Fig. 9C) is due to Si [4Si] environments and reflects the unique local geometries within the zeolite Y unit cell [90,91].

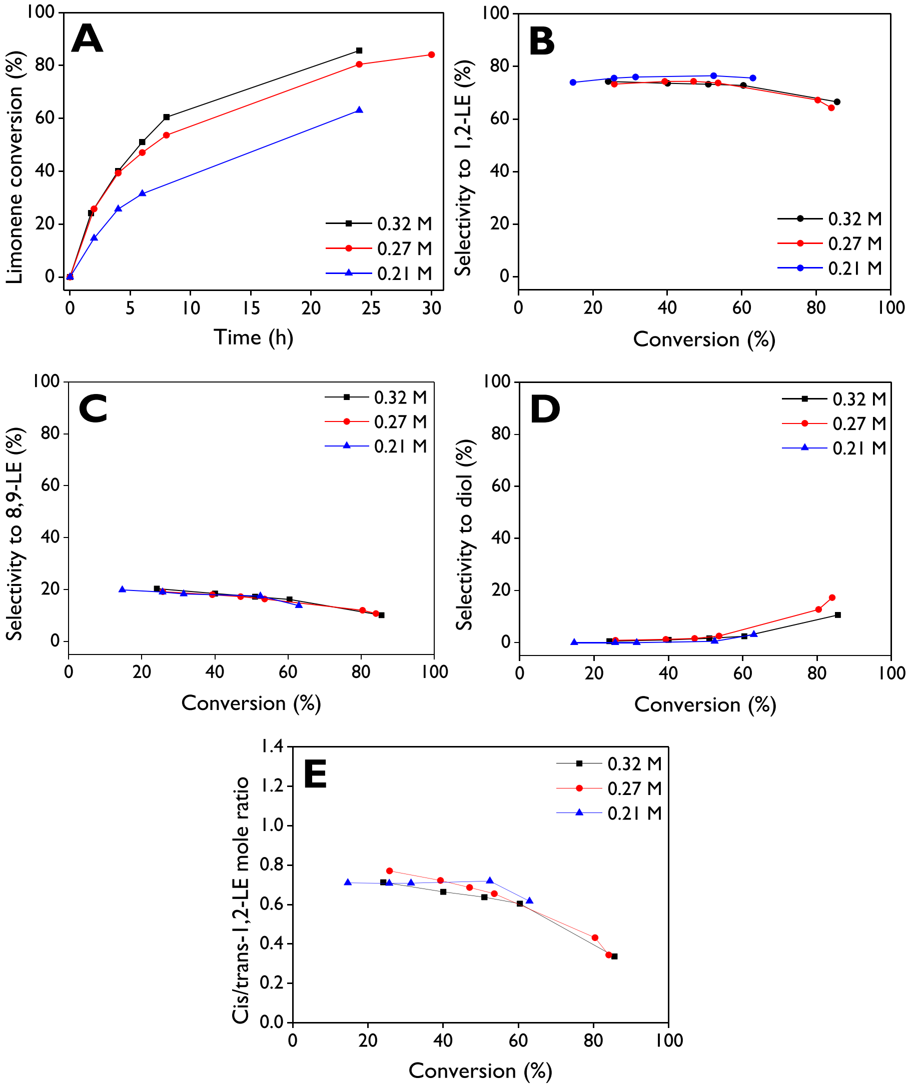

Fig. 13. Effect of the limonene initial concentration in the conversion and product distribution over KSnHYD2 as a catalyst: Limonene conversion as a function of the reaction time **(A)**; selectivity to limonene-1,2-epoxides **(B)**, selectivity to limonene-8,9-epoxides **(C)**, selectivity to limonene diol **(D)**, and *cis/trans*-limonene-1,2-epoxide molar ratio **(E)** as a function of the conversion. **Reaction conditions:** H_2O_2/limonene molar ratio = 5:1, acetonitrile as a solvent, 648 mg of catalyst, 70 °C, 800 rpm.

3.2. Catalytic performance

A preliminary study of heterogeneous catalysts, in which micro and mesoporous materials based on zeolites were investigated, revealed the modified materials on hierarchical zeolite Y as promising for the epoxidation reaction of R-(+)-limonene (Fig. S25). Therefore, these materials are further examined in this contribution. Furthermore, the repeatability of the experimental procedure was confirmed using the KSnHYD2 catalyst, as depicted in Fig. S26.

3.2.1. Initial reaction rate and turnover frequency

The initial reaction rate ($-r_{L,0}$) of R-(+)-limonene transformation and the turnover frequency (TOF) were correlated with the Brønsted/Lewis acidity mole ratio (BA/LA) and the mesoporosity fraction, as shown in Fig. 10. Fig. 10A demonstrates an inverse relationship between $-r_{L,0}$ and the BA/LA ratio, where the highest initial rates were obtained with the catalysts exhibiting the highest Sn loadings and the lowest BA/LA ratios, such as KSnHYD2 (BA/LA = 0.1) and SnHYD2 (BA/LA = 0.3), with values of 3.1 and 2.5 mmol g^{-1} h^{-1}, respectively. In contrast, the hierarchical support (HYD, BA/LA = 1.1) exhibited the lowest value, corresponding to 0.1 mmol g^{-1} h^{-1}. On the other hand, $-r_{L,0}$ exhibited a direct relationship with the mesoporosity fraction (MES), as observed in Fig. 10B. KSnHYD2 (MES = 43%) followed by SnHYD2 (MES = 31%) were the materials with the highest mesoporosity values. The other catalysts with mesoporosities between 20% and 30% exhibited the initial rates below 1.1 mmol g^{-1} h^{-1}. For TOF, similar observations regarding the BA/LA ratio (Fig. 10C) and mesoporosity (Fig. 10D) can be made, with the highest values of 96.1 and 30.2 h^{-1} for KSnHYD2 and SnHYD2, respectively. It is noteworthy that the parent zeolite (HY), while exhibiting a higher initial rate than HYD (7 times), demonstrates TOF values that are remarkably similar for both materials (2.4 and 1.3 h^{-1}). In general, high TOF and $-r_{L,0}$ values can be observed at low surface areas (Figures S27A and S27E), and low Brønsted acidity (Figure S27D and S27H). These trends are consistent, except for the hierarchical zeolite (HYD), which exhibits almost negligible activity despite its high surface area of approximately 753 m^2 g^{-1}. Furthermore, there is no clear relationship between $-r_{L,0}$ and TOF with either the total acidity of the materials (Figures S27B and S27F) or Lewis acidity (Figures S27C and S27G).

3.2.2. Conversion and product distribution

Conversion and selectivity toward the main products were

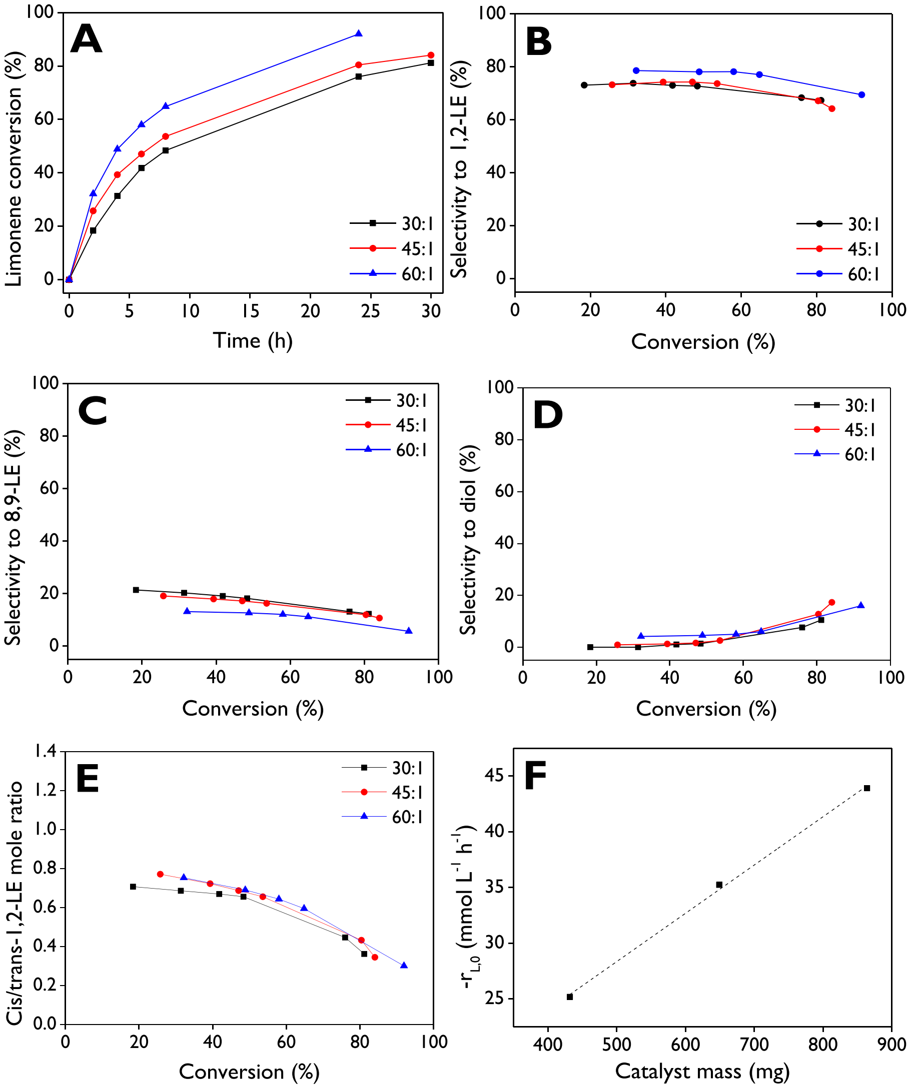

Fig. 14. Effect of the catalyst amount (catalyst (mg):limonene (mmol) ratio) in the R-(+)-limonene conversion and product distribution over KSnHYD2 as a catalyst: Limonene conversion as a function of the reaction time **(A)**; selectivity to limonene-1,2-epoxides **(B)**, selectivity to limonene-8,9-epoxides **(C)**, selectivity to limonene diol **(D)**, and *cis/trans*-limonene-1,2-epoxide molar ratio **(E)** as a function of conversion; initial reaction rate of limonene as a function of the catalyst mass **(F)**. **Reaction conditions:** $C_{L,0}$ = 0.27 M, acetonitrile as a solvent, H_2O_2/limonene molar ratio = 5:1, 70 °C, 800 rpm.

investigated with the prepared heterogeneous catalysts, as illustrated in Fig. 11. At the same reaction time, the increasing order of catalytic activity, based on conversion (Fig. 11A), was as follows: HYD < HY < SnHYD1 < KSnHYD1 < SnHYD2 < KSnHYD2. This trend aligns with the behavior of $-r_{L,0}$ and TOF represented in Fig. 10. Under the tested conditions, a conversion of ca. 76% was achieved with KSnHYD2 after 24 h. The reaction was also conducted without a catalyst (Blank), resulting in approximately 5% conversion after 24 h, attributed to the non-catalytic reaction. This emphasizes the importance of using a heterogeneous catalyst for successful epoxidation of R-(+)-limonene.

The results clearly indicate that the parent and hierarchical supports are not very active per se for the catalytic reaction. When the hierarchical support is modified with Sn and K, the activity is significantly enhanced due to modification of the physicochemical properties, as discussed previously. Selectivity to the internal epoxides with hierarchical-based catalysts exhibited values of ca. 70–80% at low conversions (Fig. 11B), which decreases as the reaction progresses, explained by formation of limonene diol (Fig. 11D) in a consecutive reaction of epoxides with water present in the commercial oxidant. In contrast, the parent zeolite (HY) exhibited the opposite behavior, increasing selectivity from 7% to 25% in the conversion range of 4–20%. Regarding selectivity to diol, it varies from 24% to 28% throughout the conversion range. On the other hand, selectivity to the external epoxides (Fig. 11C) shows very similar values of ca. 10% for all materials during the entire conversion range, except for KSnHYD2, which displayed maximum values of ca. 21% at low conversions (20%), decreasing to 12% at 80% conversion. Fig. 11E illustrates that *trans* internal epoxide is preferable compared to the *cis* configuration for the Sn- and K-modified catalyst, while for HY and HYD, the profile stabilizes at 0.33 and 0.43, respectively. Fig. 11F demonstrates that selectivity to diol is favored with high BA/LA ratios, as previously shown in the literature with hierarchical zeolites [92]. Conversely, Fig. 11G illustrates that the *cis/-trans*-1,2-LE ratio decreases as the BA/LA ratio increases but exhibits a maximum at a BA/LA of ca. 0.3. Fig. S28 shows the concentration of diol as a function of the concentration of limonene-1,2-epoxide, exhibiting a typical behavior of a consecutive reaction corresponding to the hydration of epoxides (Fig. 1).

The results obtained with metal-modified hierarchical zeolites are comparable to those reported in the literature using two double-layer hydroxides, such as ZnAl-LDH functionalized with *bis*(4- HOOC-phenyl)-acenaphthenequinonediimine) (H2BIAN) as catalysts [58], along with TBHP as the oxidizing agent. The authors reported 94% of

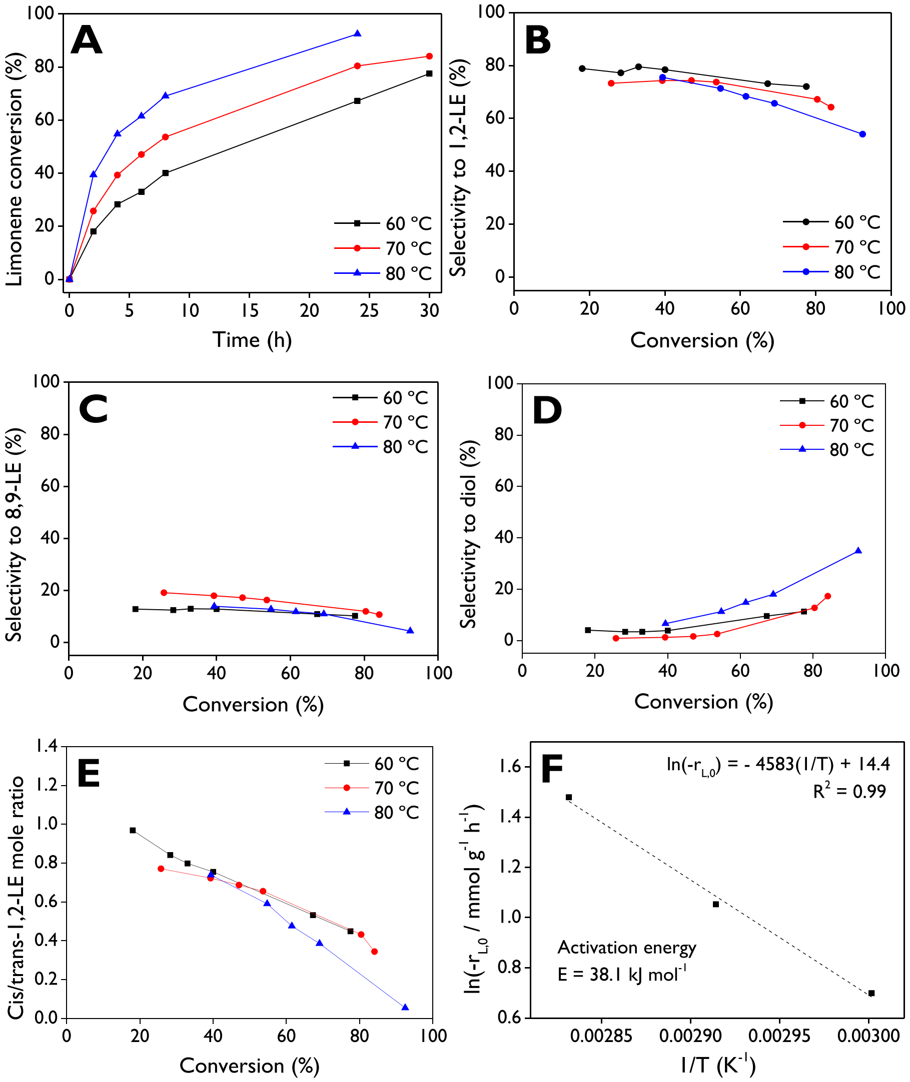

Fig. 15. Effect of the reaction temperature in the R-(+)-limonene conversion and product distribution over KSnHYD2 as a catalyst: Limonene conversion as a function of the reaction time **(A)**; selectivity to limonene-1,2-epoxides **(B)**, selectivity to limonene-8,9-epoxides **(C)**, selectivity to limonene diol **(D)**, and *cis/trans*-limonene-1,2-epoxide molar ratio **(E)** as a function of conversion; estimation of the activation energy **(F)**. **Reaction conditions:** $C_{L,0}$ = 0.27 M, acetonitrile as a solvent, H_2O_2/limonene molar ratio = 5:1, 648 mg of catalyst, 800 rpm.

Table 6
Activation energy with different heterogeneous catalysts for limonene oxidation.

Catalyst	E (kJ mol^{-1})	Reference
PW-Amberlite	76.0	[94]
MgO	52.3	[49]
Al_2O_3 (ILE)[a]	33.5	[95]
Al_2O_3 (ELE)[a]	54.4	[95]
Tungsten-based catalyst (LE)[b]	36.0	[93]
Tungsten-based catalyst (LG)[b]	79.0	[93]
Tungsten-based catalyst (LD)[b]	43.0	[93]
KSnHYD2	38.1	This work

[a] Activation energy for the transformation of limonene to internal (ILE) or external (ELE) epoxides.

[b] Activation energy for the transformation of limonene to monoepoxides (LE), limonene glycol (LG) or limonene diepoxide (LD).

conversion with 97% selectivity to monoepoxides after 24 h, as opposed to 76% and 90% achieved with KSnHYD2 in this contribution, respectively. It is worth noting that the former study employed a significantly higher temperature (110 °C) compared to 70 °C used in this contribution. Additionally, conversion and selectivity results in this study surpass those reported recently with other heterogeneous catalysts [47,50,52,62]. A catalytic system with WO_3–SiO_2 as the catalyst, dioxane and isopropanol as solvents, and H_2O_2 as the oxidant, exhibited 54% conversion after 4 h at 80 °C, with selectivity values of 53%, 33%, and 9% to monoepoxides, glycol, and allylic products, respectively [50]. The modification of zeolite Y with a complex of the type $[VO(Sal_2bz)]_2$ produced high limonene conversion (90%) after 24 h at 80 °C, using acetonitrile as a solvent, but the main products corresponded to allylic compounds and limonene glycol with selectivity values of 49% and 39%, respectively [47]. Co/SBA-16 with ethyl acetate as a solvent, and O_2 and isobutyraldehyde as oxidants, yielded almost complete limonene conversion with selectivity to monoepoxides below 50% and to diepoxide between 25% and 41% [62]. Tungstenocene (IV) dichloride was anchored on amorphous silica (W/SiO_2) and was tested on limonene oxidation using H_2O_2 as the oxidant and acetonitrile as a solvent, producing 68% conversion and 63% selectivity to monoepoxides after 6 h at 90 °C [52].

On the other hand, MgO was reported as a successful heterogeneous catalyst for the selective synthesis of monoepoxides and diepoxides, depending on the reaction conditions [49]. High yields of monoepoxides (80%) and diepoxides (96%) can be achieved after 30 min and 2 h,

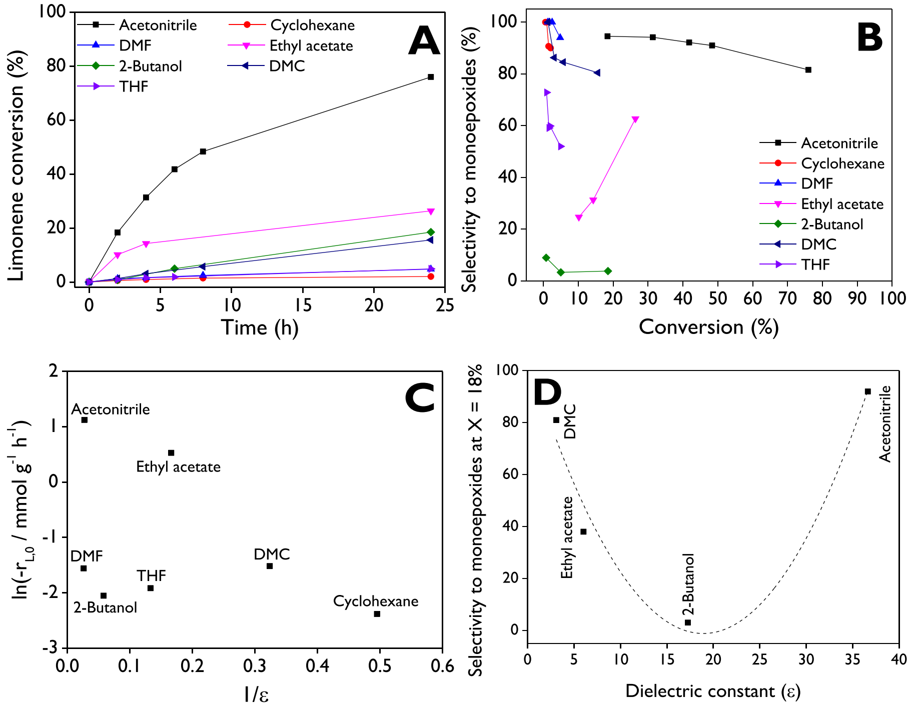

Fig. 16. Role of the solvent in the R-(+)-limonene conversion and product distribution over KSnHYD2 as a catalyst: Limonene conversion as a function of the reaction time **(A)**; selectivity to monoepoxides (internal + external) **(B)**; ln $(-r_{L0})$ of limonene as a function of 1/ε **(C);** selectivity to monoepoxides at 18% conversion as function of the dielectric constant **(D). Reaction conditions:** $C_{L,0} = 0.27$ M, H_2O_2/limonene molar ratio = 5:1, 648 mg of catalyst, 70 °C (66 °C for THF), 800 rpm.

respectively, at 50 °C. However, the catalytic system corresponds to a Payne system, which is more complex than the one used in this contribution. In this system, the oxidant intermediate, peroxyacetimidic acid, is produced from acetonitrile and H_2O_2, and the presence of water and acetone is required as solvents.

Therefore, the heterogeneous catalysts reported in this contribution and prepared based on the hierarchical zeolite Y, are promising for limonene epoxidation. Thus, as KSnHYD2 was the most active material for the epoxidation reaction, different reaction conditions were studied as discussed below.

3.2.3. Effect of the reaction conditions

The feed molar ratio of the oxidant to the substrate plays a crucial role in the epoxidation of monoterpenes, gaining even more importance when aqueous solutions of the oxidizing agent, such as H_2O_2, are used. This makes sense due to the production of limonene diepoxide is favored by higher concentrations of the oxidant in the reaction medium [49]. Additionally, higher concentration of water can lead to the undesired hydration of the internal limonene epoxides toward limonene diol, as illustrated in Fig. 1. Conversion profiles with varying the H_2O_2/limonene molar ratio at 3:1, 5:1, and 7:1 are shown in Fig. 12A. These profiles exhibit the expected behavior, with limonene conversion increasing as the oxidant amount in the reaction medium increases, reaching values of 75%, 84%, and 97%, respectively, after 30 h. The plot between ln $(-r_0)$ and ln $(C_{H2O2,0})$, illustrated in Fig. S29, exhibits a fractional reaction order of ~ 0.5, similar to previously reported [93], which suggest a complex mechanism in the transformation of limonene. Selectivity to the internal epoxides (*cis*-1,2-LE + *trans*-1,2-LE) as a function of conversion (Fig. 12B) showed that, at the same conversion, selectivity is favored at the lowest reactant ratio, yielding values of ca. 76–84% in the entire conversion range.

The selectivity profiles to external epoxides (*cis*-8,9-LE + *trans*-8,9-LE) are shown in Fig. 12C, with values below 20%, indicating no significant effect of the reactants molar ratio. Resul et al. [93] reported similar trends in the yield of monoepoxides (1,2-LE + 8,9-LE) as a function of the oxidant amount, demonstrating a preference for monoepoxides with a low amount of oxidant in the system. In coherence with the decrease of selectivity to 1,2-LE as the reaction progresses, the selectivity to diol (Fig. 12D) is favored with the highest molar ratio (7:1), reaching values about 39% at almost complete conversion, while only 7% is observed with the 3:1 ratio at 74% conversion. Similar observations were reported using a tungsten-based catalyst at 50 °C and toluene as a solvent [93]. Fig. 12E displays the molar ratio of the two isomers of the internal epoxides as a function of conversion, showing a notable predominance of the *trans* configuration over the *cis* one. Almost zero value is observed for the highest reactant ratio (7:1) at 97% conversion, and around 0.5 for the lowest one (3:1) at 74% conversion. These results could suggest a different dependence on the reaction order for the hydration of *cis* and *trans* isomers. The balance of the products corresponds to traces of allylic products such as carveol and carvone, limonene diepoxide, and dihydrocarvone as an isomer of the internal epoxides. The highest selectivity to diepoxide (~ 5%) was reached with the 5:1 ratio after 30 h.

Investigation of the initial concentration of limonene was done using the H_2O_2/limonene ratio of 5:1, chosen to prevent hydration of the internal epoxides and achieve a high yield of monoepoxides. The reaction rate generally increases as the initial substrate concentration rises, providing a straightforward explanation for the observed behavior in Fig. 13A. Limonene conversion is notably enhanced with increasing initial molar concentrations, reaching values of ca. 86% and 63% after 24 h with 0.32 M and 0.21 M, respectively. The plot between ln $(-r_0)$ and ln $(C_{L,0})$, as illustrated in Figure S30A, reveals a fractional reaction order of ~ 1.7, differing from the first-order dependence reported with a tungsten-based catalyst [93]. This once again supports the conclusion of a complex mechanism for the limonene epoxidation route over KSnHYD2 as a catalyst.

Selectivity to internal epoxides (Fig. 13B) exhibits slightly higher values at the lowest initial concentration and maintains almost constant values of ca. 74–76% across the conversion range. For concentrations of 0.27 M and 0.32 M, a similar trend is observed, with a decreasing

Table 7
Effect of different solvents in the oxidation reaction of R-(+)-limonene. Conversion and product distribution after 24 h.

Solvent	Structure	Dielectric constant[a] [99]	Dipole moment (D) [100,101]	Donor number (kcal mol^{-1}) [97]	$-r_{L,0}$ (mmol g^{-1} h^{-1})	TOF (h^{-1})	Limonene conversion (%)	Product distribution (%)
Cyclohexane	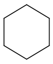	2.02	0.00	0.0	0.1	2.9	2.1	12.4 *cis*-ILE 72.2 *trans*-ILE 15.4 ELE
Dimethyl carbonate (DMC)	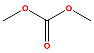	3.09[b]	0.93	17.2	0.2	6.8	15.6	36.6 *cis*-ILE 31.9 *trans*-ILE 11.9 ELE 4.1 CL 3.6 CNE 4.9 LG
Ethyl acetate	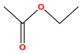	6.02[b]	1.78	17.1	1.7	53.0	26.4	24.7 *cis*-ILE 29.7 *trans*-ILE 8.3 ELE 1.4 DHC 1.6 CL 1.5 CNE 8.7 LG
Tetrahydrofuran (THF)	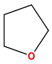	7.52	1.63	20.0	0.1	4.6	4.9	15.6 *cis*-ILE 21.1 *trans*-ILE 15.3 ELE 1.7 DHC 8.8 CL 5.9 CNE
2-Butanol	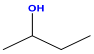	17.26	1.7	n.a	0.1	4.0	18.5	0.3 *cis*-ILE 1.6 *trans*-ILE 1.9 ELE 3.6 CL 2.9 CNE 4.5 LD 43.2 LG
Acetonitrile	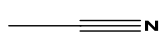	36.64	3.5	14.1	3.1	96.1	76.0	17.9 *cis*-ILE 49.5 *trans*-ILE 12.3 ELE 0.7 DHC 1.2 CL 0.6 CNE 7.3 LD 10.5 LG
N–N-Dimethylformamide (DMF)	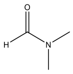	38.25	3.8	26.6	0.2	6.6	4.8	36.3 *cis*-ILE 41.5 *trans*-ILE 16.2 ELE 6.0 CNE

Reaction conditions: $C_{L,0} = 0.27$ M, H_2O_2/limonene molar ratio = 5:1, 648 mg of catalyst, 70 °C (66 °C for THF), 800 rpm. Dielectric constant reported at [a]20 °C or [b]25 °C. n.a: not available. **ILE:** Internal limonene epoxide, **ELE:** External limonene epoxide, **CL:** Carveol, **CNE:** Carvone, **DHC:** Dihydrocarvone, **LD:** Limonene diepoxide, **LG:** Limonene glycol.

selectivity attributed to the transformation of internal epoxides with water, leading to the formation of the diol. This is clearly depicted in Fig. 13D, where the maximum values of ca. 18% are observed. In contrast, selectivity to the external epoxides (Fig. 13C) demonstrates almost complete independence from the initial concentration, consistently remaining below 20% throughout the entire conversion range. Similar trends are evident in Fig. 13E for the *cis/trans* molar ratio, where values of around 0.34 are reached at 86% conversion for 0.27 M and 0.32 M, while the lowest value (0.6) corresponds to 63% conversion for 0.21 M. The maximum selectivity to limonene diepoxide (11%) was achieved with an initial concentration of 0.32 M after 24 h.

The effect of the number of active sites, directly related to the catalyst amount, was studied using different ratios of the catalyst (mg) to limonene (mmol), ranging from 30:1 to 60:1, as shown in Fig. 14. Limonene conversion of ca. 92%, 80%, and 76% was reached after 24 h using ratios of 60:1, 45:1, and 30:1, respectively, exhibiting the profiles demonstrated in Fig. 14A. On the contrary, selectivity profiles for internal epoxides (Fig. 14B), external epoxides (Fig. 14C), and diol (Fig. 14D) showed to be almost independent on catalyst mass. Fig. 14E displays that formation of *trans*-1,2-LE is more significant than *cis*-1,2-LE due to the *cis/trans* ratios below 1, which is explained by thermodynamic favorability of the *trans* configuration compared to the *cis* configuration. This is established with the binding energy of adsorption on the active sites of each configuration, with values of −2.1 kJ mol^{-1} and 5.4 kJ mol^{-1}, respectively [92]. Fig. 14F confirms that non-catalytic routes are not relevant in this system due to the linear dependence of the initial reaction rate of the substrate and the catalyst mass.

The effect of the temperature on R-(+)-limonene epoxidation was investigated within the range of 60–80 °C, as depicted in Fig. 15. Fig. 15A clearly illustrates higher limonene conversion at high temperatures, reaching 67%, 80%, and 93% after 24 h for 60 °C, 70 °C, and 80 °C, respectively. Selectivity to 1,2-LE (Fig. 15B) is negatively impacted by temperature, as selectivity decreases with the progress of the reaction. This is explained by subsequent conversion of these epoxides towards diol, as depicted in Fig. 15D. Maximum selectivity to 1,2-LE and diol correspond to 80% (33% conversion) and 35% (93% conversion), respectively, achieved at 60 °C and 80 °C. Fig. 15C reveals that selectivity to 8,9-LE remains below 20% for the three temperatures in the conversion range, with the maximum values observed at 70 °C. Similarly, in line with the profile of *cis/trans*-1,2-LE molar ratio with the highest H_2O_2/limonene ratio (7:1) in Fig. 12E, the reaction at 80 °C demonstrates a possibility of achieving a ratio close to zero at high limonene conversions (Fig. 15E). This is attributed to preferential hydration of *cis*-1,2-LE into diol. On the other hand, estimation of the activation energy of limonene epoxidation can be done using the plot of the initial reaction rate as a function of 1/T, as shown in Fig. 15F,

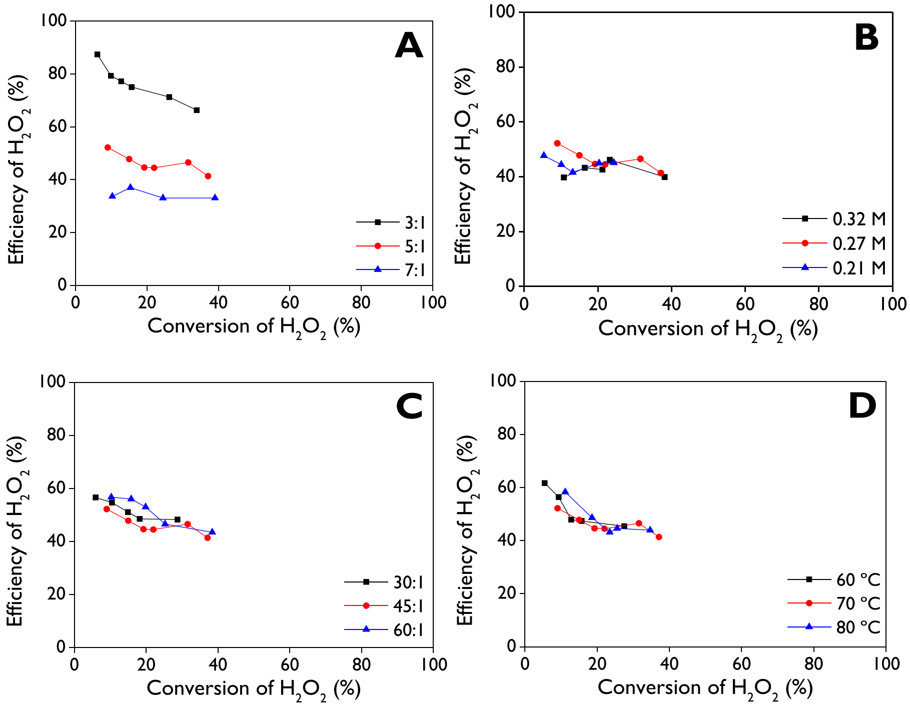

Fig. 17. Efficiency of H_2O_2: **(A)** effect of the H_2O_2/limonene molar ratio, **(B)** effect of the limonene initial concentration, **(C)** effect of the catalyst (mg): limonene (mmol) ratio, and **(D)** effect of the reaction temperature. The reaction conditions were reported in the labels of Fig. 12–15.

resulting in a value of 38.1 kJ mol^{-1}. Table 6 displays the activation energy previously reported for limonene oxidation using different heterogeneous catalysts. Notably, the estimated value in this work closely resembles two previous systems that used a homogeneous tungsten-based catalyst (36.0 kJ mol^{-1}) and Al_2O_3 (33.5 kJ mol^{-1}).

3.2.4. *Role of the solvent*

Different solvents were tested in the R-(+)-limonene epoxidation to investigate the solvent features that favor selective formation of the monoepoxides. Non-polar solvents such as cyclohexane, protic polar solvents like 2-butanol, and aprotic polar solvents including DMC, ethyl acetate, THF, acetonitrile, and DMF, were evaluated. Fig. 16A shows that acetonitrile is by far the solvent allowing the highest limonene conversion (76%) after 24 h, followed by ethyl acetate with 26%. The initial reaction rate for limonene was plotted as a function of the inverse of dielectric constant (1/ε), as shown in Fig. 16C, which clearly displays the highest catalytic activity with acetonitrile, followed by ethyl acetate. The other solvents exhibited conversion values below 20%, indicating their limitations for this heterogeneous epoxidation system. On the other hand, selectivity to the total monoepoxides (*cis*-1,2 + *trans*-1,2 + *cis*-8,9 + *trans*-8,9) as a function of conversion, given in Fig. 16B, shows values above 90% with acetonitrile for low conversions, which decreases as the reaction proceeds. This is explained by the consecutive reaction of internal monoepoxides towards diol (Fig. 12D, 13D, 14D, 15D). Additionally, the selectivity to monoepoxides at 18% conversion was plotted as a function of the dielectric constant, as shown in Fig. 16D. It exhibits a minimum around the value corresponding to 2-butanol, demonstrating a strong dependency of selectivity on solvent polarity, as has been discussed [96]. Cyclohexane, DMC, and DMF appeared to be highly selective to the reaction, being, however, not suitable solvents due to their low reactivity. THF and ethyl acetate display a wide range of selectivity values between 25% and 75% during the conversion range obtained for those solvents. Specifically, hydrophobic limonene was not easily diffused to the active site in the cyclohexane, explained by the formation of two phases with the commercial H_2O_2.

Table 7 displays the initial reaction rate of limonene, TOF, conversion, and product distribution with the studied solvents, as well as their main properties such as dielectric constant (ε), dipole moment (μ), and donor number (DN) developed by Gutmann in 1976 [97]. Limonene diol was mainly observed using 2-butanol with selectivity of 43%, making this solvent the least selective to monoepoxides (Fig. 16B). A crucial aspect to observe is the appreciable difference between the catalytic activity using acetonitrile and DMF as solvents, with TOF values of 96.1 and 6.6 h^{-1}, respectively. Both are aprotic polar solvents with very similar polarity (ε = 36.6 and 38.3 and μ = 3.5D and 3.8D); however, this difference in reactivity can be explained by the appreciable difference in the DN values, being 14.1 and 26.6 for acetonitrile and DMF, respectively, indicating that acetonitrile is a much weaker Lewis base than DMF. Furthermore, DMF is bulkier than acetonitrile, i.e., it has a larger size and more steric hindrance in comparison with acetonitrile [98]. On the other hand, the second-best solvent was ethyl acetate (Fig. 16C), which has significantly lower polarity than acetonitrile, but the DN values are quite similar (17.1 and 14.1). Therefore, these results suggest that R-(+)-limonene epoxidation over KSnHYD2 as a catalyst requires aprotic polar solvents with high polarity as well as medium donor capacity.

3.3. *Efficiency of the oxidizing agent*

H_2O_2 is consumed through two parallel reactions: its consumption in the epoxidation reaction with limonene (Eq. (9)) and its decomposition into water and oxygen (Eq. (10)).

$$C_{10}H_{16} + H_2O_2 \rightarrow \text{Products} \tag{9}$$

$$H_2O_2 \rightarrow H_2O + \frac{1}{2}O_2 \tag{10}$$

Assigning X_L as the limonene conversion (Eq. (1)), X_{ep} as the partial conversion of H_2O_2 through epoxidation reaction (Eq. (9)), and X_{dec} as the partial conversion of H_2O_2 through decomposition (Eq. (10)), Eq. (11) is used to calculate X_{ep}:

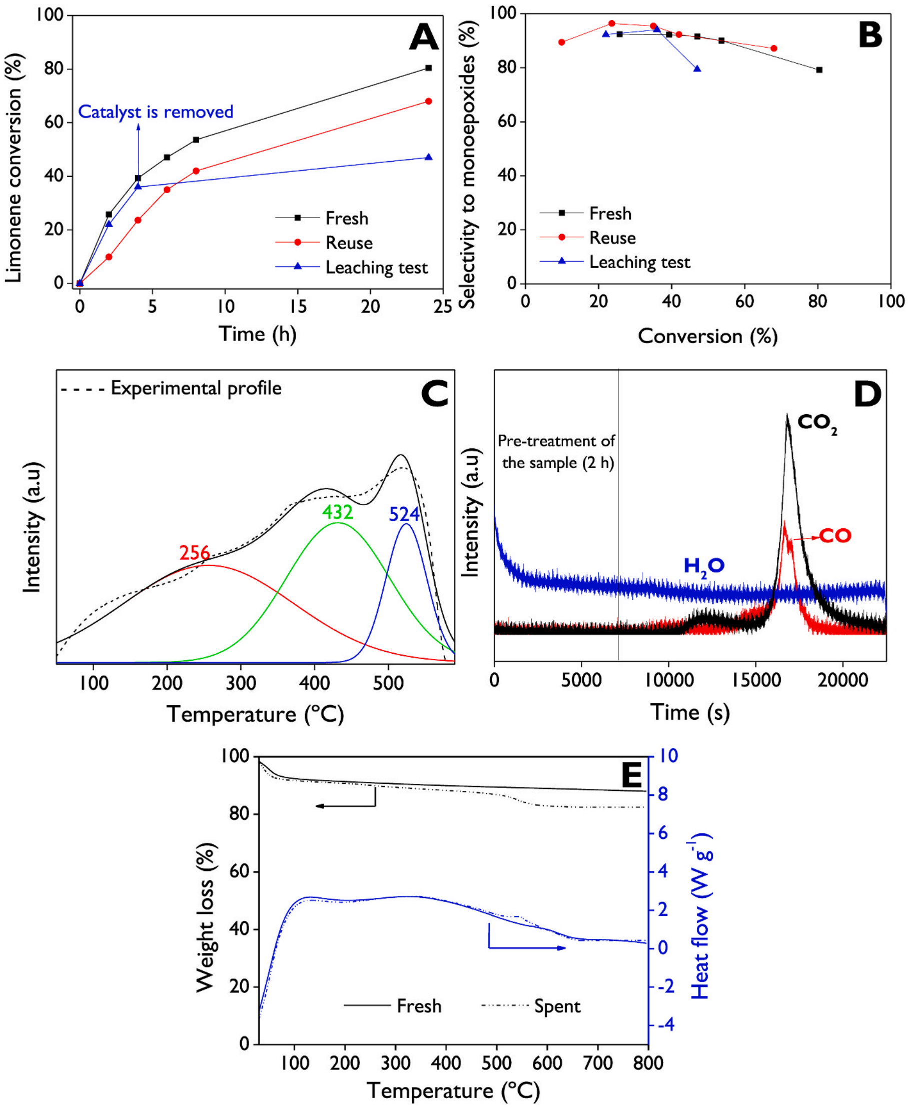

Fig. 18. **(A)** Limonene conversion as a function of time, **(B)** Selectivity to monoepoxides as a function of conversion, **(C)** O_2-TPO profile for spent KSnHYD2 catalyst, **(D)** In-situ mass spectrometry coupled with TPO, **(E)** TGA analysis for the fresh and spent KSnHYD2 catalysts.

$$C_{L,0}X_L = C_{H_2O_2,0}X_{ep} \rightarrow X_{ep} = \frac{C_{L,0}X_L}{C_{H_2O_2,0}} \tag{11}$$

X_{dec} is calculated using the overall conversion of H_2O_2 determined by cerimetric titration (Eq. (7)), as indicated in Eq. (12):

$$X_{H_2O_2} = X_{ep} + X_{dec} \tag{12}$$

The efficiency of H_2O_2 ($E_{H_2O_2}$) in the epoxidation reaction is defined according to Eq. (13):

$$E_{H_2O_2} = \frac{X_{ep}}{X_{H_2O_2}} \tag{13}$$

The profiles of H_2O_2 conversion are shown in Fig. S31, reflecting the expected behavior. The overall conversion increases with the feed H_2O_2/limonene molar ratio, limonene initial concentration, catalyst amount, and temperature, as previously reported [49]. From Figure S31D, the activation energy for the H_2O_2 decomposition was estimated to be 45.3 kJ mol^{-1}. The results concerning the efficiency of H_2O_2, presented in Fig. 17, do exhibit a strong dependence on the feed H_2O_2/limonene ratio (Fig. 17A), while not significantly affected by the initial concentration of limonene (Fig. 17B), catalyst amount (Fig. 17C), and temperature (Fig. 17D). The highest efficiency values were achieved with an H_2O_2/limonene molar ratio of 3:1, resulting in approximately 85% efficiency at low conversions, gradually decreasing to ca. 65% at 40% conversion. Under other conditions, efficiency ranged between 40% and 60%. Similar results for the efficiency of H_2O_2 in the epoxidation of R-(+)-limonene have been reported using MgO as a heterogeneous catalyst in a Payne system [49].

3.4. *Catalyst stability*

Robustness of the KSnHYD2 catalyst was investigated through reusability and leaching tests. The reuse of the catalyst was tested in the reaction after washing with acetone and regenerating the spent catalyst at 550 °C. The profiles of limonene conversion are shown in Fig. 18A. The results demonstrated conversion of ca. 68% with the reuse run after 24 h, which is slightly lower than the fresh run, corresponding to 80%. This loss of activity can be explained by the leaching test. When the catalyst was removed after 4 h of the reaction medium by the hot-filtration method and the reaction was allowed to continue, an increase of ca. 11% in conversion was obtained after 24 h. Therefore, there is a slight leaching of Sn into the reaction medium. However, the main contribution to the reaction is through heterogeneous catalysis, as depicted in the profile with the fresh run reaching high conversions compared to the leaching test.

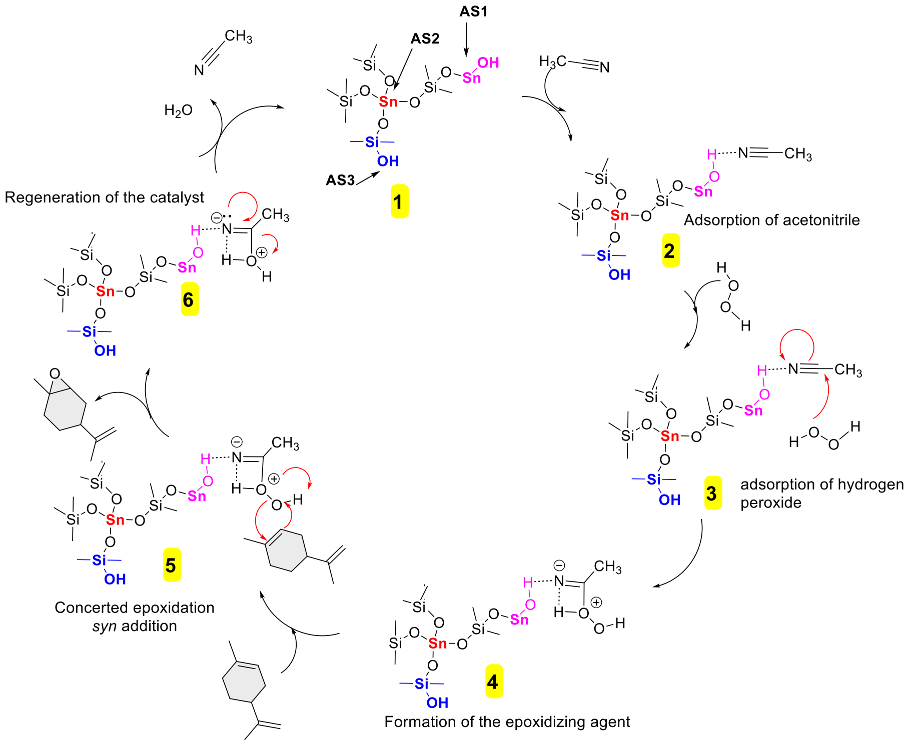

Fig. 19. Plausible reaction pathway for R-(+)-limonene epoxidation with H_2O_2.

Selectivity to total monoepoxides (Fig. 18B) looks very similar for fresh and reuse runs, although its value decays significantly when the catalyst is removed, which makes sense considering the heterogeneous catalytic nature of the reaction. Regeneration of the spent catalyst by calcination was required because TPO-MS results (Fig. 18C and 18D) confirmed coke formation, specifically a peak at 256 °C is associated with soft coke, while two peaks associated with hard coke were observed at 432 and 524 °C [102]. Similar results were obtained for the TPO-MS analysis of the spent SnHYD1 (Fig. S32), spent SnHYD2 (Fig. S33), and KSnHYD1 (Fig. S34). Once the catalyst was regenerated, no signals were observed by TPO-MS, showing the success of the procedure (Fig. S35). Furthermore, around 5.5 wt% of coke formed on the surface of spent KSnHYD2 was estimated from the TGA analysis (Fig. 18E).

3.5. Reaction pathway

A plausible reaction pathway for the epoxidation of R-(+)-limonene with H_2O_2 is proposed in Fig. 19. Three different active sites (AS1, AS2, and AS3) **(1)** are suggested based on a previous report that identified similar sites [103]. Although the presence of silanol (AS3) and internal siloxane groups is typical, they lack sufficient strength to catalyze the reaction. Consequently, the most active sites are the Sn–OH groups (AS1), which exhibit lower steric hindrance than the tetrahedral Sn sites (AS2). Therefore, AS1 can be suggested as the active site in proposed the reaction pathway. Initially, acetonitrile is adsorbed in AS1 **(2),** followed by adsorption of hydrogen peroxide **(3).** The catalyst assists in the formation of peroxyacetimidic acid as an epoxidizing agent through hydrogen bonding [49,104] **(4).** Then, limonene is presumably adsorbed onto either the internal or external double bond **(5)** undergoing concerted epoxidation with a syn addition-type, producing limonene epoxide (1,2 or 8,9). It is important to note that when H_2O_2 delivers oxygen for the epoxidation, water is generated. Subsequently, the catalyst is regenerated, along with the solvent **(6).** It is noteworthy that Fig. 19 represents a mechanistic scheme of limonene epoxidation by the internal double bond, producing limonene-1,2-epoxide. The pathway for the diepoxide is essentially the same, with the difference that in stage (5) the corresponding monoepoxide is adsorbed to produce diepoxide. Finally, limonene glycol is formed through hydration of limonene-1, 2-epoxide.

4. Conclusions

Heterogeneous catalysts based on zeolite Y were successfully evaluated for the epoxidation of R-(+)-limonene, including parent, dealuminated, Sn-modified zeolite Y, and K–Sn-modified zeolite Y with a nominal SiO_2/Al_2O_3 ratio of 30. These epoxides have gained importance due to their use as excellent building blocks in the production of bio-polycarbonates, offering attractive thermal and optical properties and avoiding the need for commercially available polyurethanes that may require toxic isocyanates for their synthesis.

Sn was incorporated using the impregnation method with $SnCl_4 \cdot 5H_2O$ as the salt precursor, and modification with K was carried out through the alkaline ion exchange method using KCl. Ordered structures were observed in all materials by XRD, with no loss of crystallinity in the hierarchical catalysts due to the dealumination process with nitric acid. SnO and SnO_2 phases were detected in the materials with the highest Sn loading (SnHYD2 and KSnHYD2). The total surface area in the catalysts decreased as the Sn loading increased, as well as when K was incorporated, suggesting pore blocking by the metal species. No structural collapse due to dealumination was confirmed by TEM and SEM analysis. The Brønsted to Lewis acidity ratio increased in the order KSnHYD2 < SnHYD2 < KSnHYD1 < SnHYD1 < HYD < HY. The total acidity of the catalysts was directly correlated using NH_3-TPD and pyridine-FTIR, while no basicity was observed in the K-modified catalysts. Isolated Sn^{4+} species in tetrahedral coordination inside the mesoporous channels were observed only in materials with high Sn loadings, while extra-framework Sn species were observed in all catalysts. Al entities with four-coordinated framework and six-coordinated extra-framework were observed by NMR.

The highest initial reaction rate (3.1 mmol g^{-1} h^{-1}) and the highest turnover frequency (96.1 h^{-1}) were obtained with KSnHYD2 zeolite, exhibiting the lowest Brønsted to Lewis acidity ratio (0.1), the highest mesoporosity fraction (43%), and the lowest total surface area (465 m^2 g^{-1}). However, no direct relationship was observed with the total surface area. The parent and dealuminated zeolites exhibited low catalytic activity, as reflected in the reaction rate and TOF. Limonene conversion increased with a higher H_2O_2/limonene molar ratio or temperature, but the opposite effect was observed for the selectivity to limonene-1,2-epoxides, indicating a preference for their hydration towards limonene diol under those conditions. Additionally, conversion was positively affected by the initial concentration of the substrate, although selectivity to the main products did not change significantly. The activation energy for the R-(+)-limonene epoxidation was estimated to be 38.1 kJ mol^{-1}. The solvent played a critical role in the epoxidation route, showing a preference for aprotic polar solvents with high polarity and medium donor capacity, such as acetonitrile, and to a lesser extent, ethyl acetate.

The efficiency of H_2O_2 in the epoxidation reaction reached maximum values of up to 85% when employing low H_2O_2/limonene molar ratios (3:1). However, a weak dependence was observed with other parameters such as temperature, initial concentration of limonene, and the catalyst amount. The activation energy for the H_2O_2 decomposition was estimated in 45.3 kJ mol^{-1}. A coke layer, constituting 5.5 wt%, formed on the catalyst surface after reaction at 70 °C. Regeneration was achieved through calcination at 550 °C. The regenerated catalyst was reused in the limonene epoxidation, demonstrating a conversion loss of ca. 12% after 24 h of the reaction, attributed to slight leaching of the catalyst into the reaction medium. In summary, valuable insights have been gained into the intricate correlation between the structure and catalytic activity of heterogeneous catalysts prepared based on hierarchical zeolite Y, which are easily synthesized being also rather robust. Moreover, these materials produced high limonene conversion (>80%) and high selectivity to monoepoxides (>90%) under different conditions, surpassing the results reported previously in the literature with many heterogeneous catalysts. Those catalysts often showed a competitive transformation between epoxidation (to monoepoxides as well as diepoxides), hydration, and the allylic route.

CRediT authorship contribution statement

Luis A. Gallego-Villada: Writing – original draft, Methodology, Investigation, Formal analysis. **Päivi Mäki-Arvela:** Writing – review & editing, Formal analysis, Conceptualization. **Narendra Kumar:** Supervision, Formal analysis, Conceptualization. **Edwin A. Alarcón:** Supervision, Funding acquisition. **Zuzana Vajglová:** Investigation. **Teija Tirri:** Supervision, Resources. **Ilari Angervo:** Investigation. **Robert Lassfolk:** Investigation. **Mika Lastusaari:** Investigation. **Dmitry Yu Murzin:** Writing – review & editing, Resources, Conceptualization.

Declaration of competing interest

The authors declare that they have no known competing financial interests or personal relationships that could have appeared to influence the work reported in this paper.

Data availability

Data will be made available on request.

Acknowledgments

The authors thank the Universidad de Antioquia for providing financial resources for this work through the project 2022–53000: “Transformation of monoterpenes through one-pot reactions over heterogeneous catalysts”, as part of the 2021–2022 Programmatic Call: Engineering and Technology. They also thank the Foundation for the Promotion of Research and Technology, project 2022–56550. Additionally, Luis A. Gallego-Villada is grateful to the Universidad de Antioquia for supporting his Ph.D. studies through the “Beca Doctoral Universidad de Antioquia” scholarship. The authors would like to express their gratitude to Dr. Julián Sánchez for his valuable advice on the reaction pathway.

Appendix A. Supplementary data

Supplementary data to this article can be found online at https://doi.org/10.1016/j.micromeso.2024.113098.

References

[1] C.H. Bartholomew, R.J. Farrauto, Fundamentals of Industrial Catalytic Processes, 1997.

[2] G. Aguirre-Cruz, F. Legorreta-Garcia, G. Aguirre-Cruz, L. Stanciu, G. Aguirre-Alvarez, Synthesis of hierarchical silica zeolites for heterogenous catalysis and adsorption, Microporous Mesoporous Mater. 345 (2022) 112274, https://doi.org/10.1016/j.micromeso.2022.112274.

[3] T. Maesen, The zeolite scene - an overview, in: J. Cejka, H. Van Bekkum, A. Corma, F. Schüth (Eds.), Introd. To Zeolite Sci. Pract., third ed., Elsevier, 2007, p. 455.

[4] L.B. McCusker, C. Baerlocher, Zeolite structures, in: J. Cejka, H. Van Bekkum, A. Corma, F. Schüth (Eds.), Stud. Surf. Sci. Catal., third ed., Elsevier, 2007, pp. 13–37, https://doi.org/10.1016/S0167-2991(07)80790-7.

[5] R. Srivastava, Synthesis and applications of ordered and disordered mesoporous zeolites: present and future prospective, Catal. Today 309 (2018) 172–188, https://doi.org/10.1016/j.cattod.2017.08.017.

[6] B.K. Singh, Y. Kim, S. Kwon, K. Na, Synthesis of mesoporous zeolites and their opportunities in heterogeneous catalysis, Catalysts 11 (2021) 1541, https://doi.org/10.3390/catal11121541.

[7] J. Liu, H. Zhang, N. Lu, X. Yan, B. Fan, R. Li, Influence of acidity of mesoporous ZSM-5-supported Pt on naphthalene hydrogenation, Ind. Eng. Chem. Res. 59 (2020) 1056–1064, https://doi.org/10.1021/acs.iecr.9b04411.

[8] T. Weissenberger, R. Leonhardt, B.A. Zubiri, M. Pitínová-Štekrová, T.L. Sheppard, B. Reiprich, J. Bauer, R. Dotzel, M. Kahnt, A. Schropp, C.G. Schroer, J. Grunwaldt, J.L. Casci, J. Čejka, E. Spiecker, W. Schwieger, Synthesis and characterisation of hierarchically structured titanium silicalite-1 zeolites with large intracrystalline macropores, Chem. Eur J. 25 (2019) 14430–14440, https://doi.org/10.1002/chem.201903287.

[9] V. Smeets, E.M. Gaigneaux, D.P. Debecker, Hierarchical micro-/macroporous TS-1 zeolite epoxidation catalyst prepared by steam assisted crystallization, Microporous Mesoporous Mater. 293 (2020) 109801, https://doi.org/10.1016/j.micromeso.2019.109801.

[10] S.P. Nandala, A. Tallam, N. Roy Choudhary, S. Sundergopal, S.K. Bhargava, Design and optimization of multilayer composite membrane for biomethane enrichment: process simulations and economics, Sep. Purif. Technol. 319 (2023) 124073, https://doi.org/10.1016/j.seppur.2023.124073.

[11] R. Wijiyanti, I.S. Caralin, A.R. Widyanto, T. Gunawan, Z.A. Karim, A.F. Ismail, M. Nomura, N. Widiastuti, Evaluation of different carbon-modified zeolite derivatives preparation methods as a filler in mixed matrix membrane on their gas separation performance, Microporous Mesoporous Mater. 359 (2023) 112650, https://doi.org/10.1016/j.micromeso.2023.112650.

[12] B. Yu, H. Deng, Y. Lu, T. Pan, W. Shan, H. He, Adsorptive interaction between typical VOCs and various topological zeolites: mixture effect and mechanism, J. Environ. Sci. 136 (2024) 626–636, https://doi.org/10.1016/j.jes.2023.02.015.

[13] Y. Tadayon, M.E. Bahrololoom, S. Javadpour, An experimental study of sunflower seed husk and zeolite as adsorbents of Ni(II) ion from industrial wastewater, Water Resour. Ind. 30 (2023) 100214, https://doi.org/10.1016/j.wri.2023.100214.

[14] A.M. Alotaibi, A.F. Ismail, E.S. Aziman, Ultra-effective modified clinoptilolite adsorbent for selective thorium removal from radioactive residue, Sci. Rep. 13 (2023) 9316, https://doi.org/10.1038/s41598-023-36487-5.

[15] W. Liu, X. Liu, Y. Gu, Y. Liu, Z. Yu, Y. Lyu, Y. Tian, A new composite consisting of Y zeolite and ZrO2 for fluid catalytic cracking reaction, Composites, Part B 200 (2020) 108317, https://doi.org/10.1016/j.compositesb.2020.108317.

[16] K. Wang, F. Wang, Y. Zhai, J. Wang, X. Zhang, M. Li, L. Jiang, X. Fan, C. Bing, J. Zhang, X. Zhang, Application of zeolite in Beckmann rearrangement of cyclohexanone oxime, Mol. Catal. 535 (2023) 112881, https://doi.org/10.1016/j.mcat.2022.112881.

[17] S.-W. Cao, P. Xiao, J. Wang, Y. Sun, Y.-S. Shang, Y.-F. Ge, Q. Liu, Y.-J. Gong, G. Mo, Z.-H. Li, Active precursor promoting nucleation/growth of MWW zeolite and controlling its morphology, Petrol. Sci. 20 (2023) 1922–1933, https://doi.org/10.1016/j.petsci.2023.01.005.

[18] A.A. Zaidi, A. Khan, H. AlMohamadi, M.W. Anjum, I. Ali, S.R. Naqvi, S. Kokuryo, K. Miyake, N. Nishiyama, Catalytic pyrolysis of rice husk over defect-rich beta zeolites for biofuel production, Fuel 348 (2023) 128624, https://doi.org/10.1016/j.fuel.2023.128624.

[19] Q. Deng, H. Peng, Z. Yang, T. Wang, J. Wang, Z. Zeng, S. Dai, A one-pot synthesis of high-density biofuels through bifunctional mesoporous zeolite-encapsulated Pd catalysts, Appl. Catal. B Environ. 337 (2023) 122982, https://doi.org/10.1016/j.apcatb.2023.122982.

[20] W. Hunsiri, N. Chaihad, C. Ngamcharussrivichai, D.N. Tungasmita, P. Reubroycharoen, N. Hinchiranan, Branched-chain biofuels derived from hydroisomerization of palm olein using Ni/modified beta zeolite catalysts for

biojet fuel production, Fuel Process. Technol. 248 (2023) 107825, https://doi.org/10.1016/j.fuproc.2023.107825.

[21] G. Papanikolaou, D. Chillè, S. Perathoner, G. Centi, M. Migliori, G. Giordano, P. Lanzafame, Use of zeolites in green chemicals and bio-fuel production via HMF valorisation, Microporous Mesoporous Mater. 358 (2023) 112330, https://doi.org/10.1016/j.micromeso.2022.112330.

[22] Z. Vajglová, N. Kumar, P. Mäki-Arvela, K. Eränen, M. Peurla, L. Hupa, M. Nurmi, M. Toivakka, D.Y. Murzin, Synthesis and physicochemical characterization of shaped catalysts of β and Y zeolites for cyclization of citronellal, Ind. Eng. Chem. Res. 58 (2019) 18084–18096, https://doi.org/10.1021/acs.iecr.9b02829.

[23] P. Mäki-Arvela, I. Simakova, Z. Vajglová, D.Y. Murzin, One-pot synthesis of menthol from citral and citronellal over heterogeneous catalysts, Catal. Surv. Asia 27 (2023) 2–19, https://doi.org/10.1007/s10563-022-09376-6.

[24] M. Laluc, R. Barakov, P. Mäki-Arvela, N. Shcherban, D.Y. Murzin, Catalytic activity of hierarchical beta zeolites in the Prins cyclization of (−)-isopulegol with acetone, Appl. Catal. Gen. 618 (2021) 118131, https://doi.org/10.1016/j.apcata.2021.118131.

[25] R. Barakov, N. Shcherban, P. Mäki-Arvela, P. Yaremov, I. Bezverkhyy, J. Wärnå, D.Y. Murzin, Hierarchical beta zeolites as catalysts in α-pinene oxide isomerization, ACS Sustain. Chem. Eng. 10 (2022) 6642–6656, https://doi.org/10.1021/acssuschemeng.2c00441.

[26] N. Shcherban, R. Barakov, B. Lasne, P. Mäki-Arvela, M. Shamzhy, I. Bezverkhyy, J. Wärnå, D.Y. Murzin, Florol synthesis via Prins cyclization over hierarchical beta zeolites, Mol. Catal. 531 (2022) 112683, https://doi.org/10.1016/j.mcat.2022.112683.

[27] B. Lasne, P. Mäki-Arvela, A. Aho, Z. Vajglova, K. Eränen, N. Kumar, J.E. Sánchez-Velandia, M. Peurla, C. Mondelli, J. Pérez-Ramírez, D.Y. Murzin, Synthesis of Florol via Prins cyclization over heterogeneous catalysts, J. Catal. 405 (2022) 288–302, https://doi.org/10.1016/j.jcat.2021.12.008.

[28] I., Future Market Insights, Fine Chemicals Market Outlook, 2023 to 2033), (2023. https://www.futuremarketinsights.com/reports/fine-chemicals-market. (Accessed 14 July 2023).

[29] R.A. Sheldon, M.L. Bode, S.G. Akakios, Metrics of green chemistry: waste minimization, Curr. Opin. Green Sustainable Chem. 33 (2022) 100569, https://doi.org/10.1016/j.cogsc.2021.100569.

[30] Knoema, Citrus fruit production by country. https://knoema.com/atlas/topics/Agriculture/Crops-Production-Quantity-tonnes/Citrus-fruit-production, 2021. (Accessed 19 July 2023).

[31] S. Suri, A. Singh, P.K. Nema, Current applications of citrus fruit processing waste: a scientific outlook, Appl. Food Res. 2 (2022) 100050, https://doi.org/10.1016/j.afres.2022.100050.

[32] E. Louisy, V. Khodyrieva, S. Olivero, V. Michelet, A. Mija, Use of limonene epoxides and derivatives as promising monomers for biobased polymers, Chempluschem 87 (2022) 1–9, https://doi.org/10.1002/cplu.202200190.

[33] J.R. Ayala, G. Montero, M.A. Coronado, C. García, M.A. Curiel-Alvarez, J.A. León, C.A. Sagaste, D.G. Montes, Characterization of orange peel waste and valorization to obtain reducing sugars, Molecules 26 (2021) 1348, https://doi.org/10.3390/molecules26051348.

[34] S. Nikfar, A.F. Behboudi, Limonene, in: Encycl. Toxicol., Elsevier, 2014, pp. 78–82, https://doi.org/10.1016/B978-0-12-386454-3.00628-X.

[35] O. Hauenstein, S. Agarwal, A. Greiner, Bio-based polycarbonate as synthetic toolbox, Nat. Commun. 7 (2016) 11862, https://doi.org/10.1038/ncomms11862.

[36] O. Hauenstein, M. Reiter, S. Agarwal, B. Rieger, A. Greiner, Bio-based polycarbonate from limonene oxide and CO2 with high molecular weight, excellent thermal resistance, hardness and transparency, Green Chem. 18 (2016) 760–770, https://doi.org/10.1039/C5GC01694K.

[37] V. Schimpf, B.S. Ritter, P. Weis, K. Parison, R. Mülhaupt, High purity limonene dicarbonate as versatile building block for sustainable non-isocyanate polyhydroxyurethane thermosets and thermoplastics, Macromolecules 50 (2017) 944–955, https://doi.org/10.1021/acs.macromol.6b02460.

[38] T. Stößer, C. Li, J. Unruangsri, P.K. Saini, R.J. Sablong, M.A.R. Meier, C. K. Williams, C. Koning, Bio-derived polymers for coating applications: comparing poly(limonene carbonate) and poly(cyclohexadiene carbonate), Polym. Chem. 8 (2017) 6099–6105, https://doi.org/10.1039/C7PY01223C.

[39] S. Kernbichl, B. Rieger, Aliphatic polycarbonates derived from epoxides and CO2: a comparative study of poly(cyclohexene carbonate) and poly(limonene carbonate), Polymer (Guildf). 205 (2020) 122667, https://doi.org/10.1016/j.polymer.2020.122667.

[40] S. Neumann, S.B. Däbritz, S.E. Fritze, L.-C. Leitner, A. Anand, A. Greiner, S. Agarwal, Sustainable block copolymers of poly(limonene carbonate), Polym. Chem. 12 (2021) 903–910, https://doi.org/10.1039/D0PY01685C.

[41] A. Rehman, A.M. López Fernández, M.F.M. Gunam Resul, A. Harvey, Highly selective, sustainable synthesis of limonene cyclic carbonate from bio-based limonene oxide and CO2: a kinetic study, J. CO2 Util. 29 (2019) 126–133, https://doi.org/10.1016/j.jcou.2018.12.001.

[42] K.A. Maltby, M. Hutchby, P. Plucinski, M.G. Davidson, U. Hintermair, Selective catalytic synthesis of 1,2- and 8,9-cyclic limonene carbonates as versatile building blocks for novel hydroxyurethanes, Chem. Eur J. 26 (2020) 7405–7415, https://doi.org/10.1002/chem.201905561.

[43] V.M. Vaschetti, G.A. Eimer, A.L. Cánepa, S.G. Casuscelli, Catalytic performance of V-MCM-41 nanocomposites in liquid phase limonene oxidation: vanadium leaching mitigation, Microporous Mesoporous Mater. 311 (2021) 110678, https://doi.org/10.1016/j.micromeso.2020.110678.

[44] A. Wróblewska, J. Serafin, A. Gawarecka, P. Miądlicki, K. Urbaś, Z.C. Koren, J. Llorca, B. Michalkiewicz, Carbonaceous catalysts from orange pulp for limonene oxidation, Carbon Lett. 30 (2020) 189–198, https://doi.org/10.1007/s42823-019-00084-2.

[45] A. Wróblewska, M. Malko, M. Walasek, Environmental friendly method of the epoxidation of limonene with hydrogen peroxide over the Ti-SBA-15 catalyst, Pol. J. Chem. Technol. 20 (2018) 6–12, https://doi.org/10.2478/pjct-2018-0047.

[46] V.M. Vaschetti, A.L. Cánepa, D. Barrera, K. Sapag, G.A. Eimer, S.G. Casuscelli, Limonene oxyfunctionalization over Cu-modified silicates employing hydrogen peroxide and t-Butyl hydroperoxide: reaction pathway analysis, Mol. Catal. 481 (2020) 110234, https://doi.org/10.1016/j.mcat.2018.11.005.

[47] D.K. Parmar, P.M. Butani, N.J. Thumar, P.M. Jasani, R.V. Padaliya, P. R. Sandhiya, H.D. Nakum, M.N. Khan, D. Makwana, Oxy-functionalization of olefins with neat and heterogenized binuclear V(IV)O and Fe(II) complexes: effect of steric hindrance on product selectivity and output in homogeneous and heterogeneous phase, Mol. Catal. 474 (2019) 110424, https://doi.org/10.1016/j.mcat.2019.110424.

[48] Y. Wang, F. Gayet, P. Guillo, D. Agustin, Organic solvent-free olefins and alcohols (ep)oxidation using recoverable catalysts based on [PM12O40]3− (M = Mo or W) ionically grafted on amino functionalized silica nanobeads, Materials 12 (2019) 3278, https://doi.org/10.3390/ma12203278.

[49] L.A. Gallego-Villada, E.A. Alarcón, A.L. Villa, Versatile heterogeneous catalytic system for the selective synthesis of limonene epoxide and diepoxide, Ind. Eng. Chem. Res. 62 (2023) 20152–20169, https://doi.org/10.1021/acs.iecr.3c02633.

[50] Y. Tao, O. De Luca, B. Singh, A.J. Kamphuis, J. Chen, P. Rudolf, P.P. Pescarmona, WO3–SiO2 nanomaterials synthesized using a novel template-free method in supercritical CO2 as heterogeneous catalysts for epoxidation with H2O2, Mater. Today Chem. 18 (2020) 100373, https://doi.org/10.1016/j.mtchem.2020.100373.

[51] W. Lueangchaichaweng, B. Singh, D. Mandelli, W.A. Carvalho, S. Fiorilli, P. P. Pescarmona, High surface area, nanostructured boehmite and alumina catalysts: synthesis and application in the sustainable epoxidation of alkenes, Appl. Catal. Gen. 571 (2019) 180–187, https://doi.org/10.1016/j.apcata.2018.12.017.

[52] C. Bisio, A. Gallo, R. Psaro, C. Tiozzo, M. Guidotti, F. Carniato, Tungstenocene-grafted silica catalysts for the selective epoxidation of alkenes, Appl. Catal. Gen. 581 (2019) 133–142, https://doi.org/10.1016/j.apcata.2019.05.027.

[53] D. Hu, X. Song, S. Wu, X. Yang, H. Zhang, X. Chang, M. Jia, Solvothermal synthesis of Co-substituted phosphomolybdate acid encapsulated in the UiO-66 framework for catalytic application in olefin epoxidation, Chin. J. Catal. 42 (2021) 356–366, https://doi.org/10.1016/S1872-2067(20)63665-8.

[54] T.R. Amarante, P. Neves, F.A. Almeida Paz, A.C. Gomes, M. Pillinger, A. A. Valente, I.S. Gonçalves, Heterogeneous catalysis with an organic–inorganic hybrid based on MoO 3 chains decorated with 2,2′-biimidazole ligands, Catal. Sci. Technol. 11 (2021) 2214–2228, https://doi.org/10.1039/D1CY00055A.

[55] S.R. Leandro, A.C. Mourato, U. Łapińska, O.C. Monteiro, C.I. Fernandes, P.D. Vaz, C.D. Nunes, Exploring bulk and colloidal Mg/Al hydrotalcite–Au nanoparticles hybrid materials in aerobic olefin epoxidation, J. Catal. 358 (2018) 187–198, https://doi.org/10.1016/j.jcat.2017.12.014.

[56] M. Fadaei Sarabi, A. Bezaatpour, A. Mahmoudi, Anchoring of a terpyridine-based Mo(VI) complex on manganese ferrite as a recoverable catalyst for epoxidation of olefins under solvent-free conditions, J. Coord. Chem. 74 (2021) 1597–1612, https://doi.org/10.1080/00958972.2021.1904507.

[57] M.S. Nunes, D.M. Gomes, A.C. Gomes, P. Neves, R.F. Mendes, F.A.A. Paz, A. D. Lopes, A.A. Valente, I.S. Gonçalves, M. Pillinger, A 5-(2-pyridyl)tetrazolate complex of molybdenum(VI), its structure, and transformation to a molybdenum oxide-based hybrid heterogeneous catalyst for the epoxidation of olefins, Catalysts 11 (2021) 1407, https://doi.org/10.3390/catal11111407.

[58] J. Marreiros, M. Diaz-Couce, M.J. Ferreira, P.D. Vaz, M.J. Calhorda, C.D. Nunes, Synthesis and catalytic activity of Mo(II) complexes of α-diimines intercalated in layered double hydroxides, Inorg. Chim. Acta. 486 (2019) 274–282, https://doi.org/10.1016/j.ica.2018.10.062.

[59] D.P. Gomes, A.F. Silva, A.C. Gomes, P. Neves, A.A. Valente, I.S. Gonçalves, M. Pillinger, Epoxidation catalysts prepared by encapsulation of molybdenum hexacarbonyl in UiO-66(Zr/Hf)-type metal-organic frameworks, Microporous Mesoporous Mater. 330 (2022) 111603, https://doi.org/10.1016/j.micromeso.2021.111603.

[60] H. Zhang, X. Lu, L. Yang, Y. Hu, M. Yuan, C. Wang, Q. Liu, F. Yue, D. Zhou, Q. Xia, Efficient air epoxidation of cycloalkenes over bimetal-organic framework ZnCo-MOF materials, Mol. Catal. 499 (2021) 111300, https://doi.org/10.1016/j.mcat.2020.111300.

[61] S. Madadi, S. Kaliaguine, Activated carbon-supported ruthenium as a catalyst for the solvent- and initiator-free aerobic epoxidation of limonene, ACS Sustain. Chem. Eng. 9 (2021) 10557–10568, https://doi.org/10.1021/acssuschemeng.1c02597.

[62] S. Madadi, L. Charbonneau, J.-Y. Bergeron, S. Kaliaguine, Aerobic epoxidation of limonene using cobalt substituted mesoporous SBA-16 Part 1: optimization via Response Surface Methodology (RSM), Appl. Catal. B Environ. 260 (2020) 118049, https://doi.org/10.1016/j.apcatb.2019.118049.

[63] A. Gottuso, A. Köckritz, M.L. Saladino, F. Armetta, C. De Pasquale, G. Nasillo, F. Parrino, Catalytic and photocatalytic epoxidation of limonene: using mesoporous silica nanoparticles as functional support for a Janus-like approach, J. Catal. 391 (2020) 202–211, https://doi.org/10.1016/j.jcat.2020.08.025.

[64] L. Charbonneau, X. Foster, D. Zhao, S. Kaliaguine, Catalyst-free epoxidation of limonene to limonene dioxide, ACS Sustain. Chem. Eng. 6 (2018) 5115–5121, https://doi.org/10.1021/acssuschemeng.7b04782.

[65] L. Charbonneau, S. Kaliaguine, Epoxidation of limonene over low coordination Ti in Ti- SBA-16, Appl. Catal. Gen. 533 (2017) 1–8, https://doi.org/10.1016/j.apcata.2017.01.001.

[66] D.M. Gomes, P. Neves, M.M. Antunes, A.J.S. Fernandes, M. Pillinger, A. A. Valente, Post-synthesis strategies to prepare mesostructured and hierarchical silicates for liquid phase catalytic epoxidation, Catalysts 12 (2022) 1513, https://doi.org/10.3390/catal12121513.

[67] E. Niño-Arrieta, A.L. Villa-Holguín, E.A. Alarcón-Durango, A. Talavera-López, S. A. Gómez-Torres, G.A. Fuentes-Zurita, Limonene epoxidation in aqueous phase over TiKIT-6, Rev. Fac. Ing. Univ. Antioquia (2018) 74–79, https://doi.org/10.17533/udea.redin.n88a08.

[68] P. Tao, X. Lu, H. Zhang, R. Jing, F. Huang, S. Wu, D. Zhou, Q. Xia, Enhanced activity of microwave-activated CoOx/MOR catalyst for the epoxidation of α-pinene with air, Mol. Catal. 463 (2019) 8–15, https://doi.org/10.1016/j.mcat.2018.11.006.

[69] J.M. Jimenez-Martin, A. Orozco-Saumell, H. Hernando, M. Linares, R. Mariscal, M. López Granados, A. García, J. Iglesias, Efficient conversion of glucose to methyl lactate with Sn-usy: retro-aldol activity promotion by controlled ion exchange, ACS Sustain. Chem. Eng. 10 (2022) 8885–8896, https://doi.org/10.1021/acssuschemeng.2c01987.

[70] L. Lutterotti, Total pattern fitting for the combined size–strain–stress–texture determination in thin film diffraction, Nucl. Instrum. Methods Phys. Res. Sect. B Beam Interact. Mater. Atoms 268 (2010) 334–340, https://doi.org/10.1016/j.nimb.2009.09.053.

[71] C.A. Emeis, Determination of integrated molar extinction coefficients for infrared absorption bands of pyridine adsorbed on solid acid catalysts, J. Catal. 141 (1993) 347–354, https://doi.org/10.1006/jcat.1993.1145.

[72] F.P. Greenspan, D.G. MacKellar, Analysis of aliphatic per acids, Anal. Chem. 20 (1948) 1061–1063, https://doi.org/10.1021/ac60023a020.

[73] IZA Structure Commission, FAU: framework type. https://europe.iza-structure.org/IZA-SC/framework.php?STC=FAU. (Accessed 26 November 2023).

[74] A. Mekki, A. Benmaati, A. Mokhtar, M. Hachemaoui, F. Zaoui, H. Habib Zahmani, M. Sassi, S. Hacini, B. Boukoussa, Michael addition of 1,3-dicarbonyl derivatives in the presence of zeolite Y as an heterogeneous catalyst, J. Inorg. Organomet. Polym. Mater. 30 (2020) 2323–2334, https://doi.org/10.1007/s10904-019-01424-5.

[75] P. Mäki-Arvela, N. Kumar, S.F. Diáz, A. Aho, M. Tenho, J. Salonen, A. Leino, K. Kordás, P. Laukkanen, J. Dahl, I. Sinev, T. Salmi, D.Y. Murzin, Isomerization of β-pinene oxide over Sn-modified zeolites, J. Mol. Catal. Chem. 366 (2013) 228–237, https://doi.org/10.1016/j.molcata.2012.09.028.

[76] M.A. Farrukh, H.B. Teck, R. Adnan, Surfactant-controlled aqueous synthesis of SnO2 nanoparticles via the hydrothermal and conventional heating methods, Turk. J. Chem. 34 (2010) 537–550, https://doi.org/10.3906/kim-1001-466.

[77] K.S.W. Sing, Reporting physisorption data for gas/solid systems with special reference to the determination of surface area and porosity (Recommendations 1984), Pure Appl. Chem. 57 (1985) 603–619, https://doi.org/10.1351/pac198557040603.

[78] V. Palomba, A. Frazzica, Modeling of sorption systems for thermal energy storage, in: Adv. Therm. Energy Storage Syst., Elsevier, 2021, pp. 453–475, https://doi.org/10.1016/B978-0-12-819885-8.00015-2.

[79] L.A. Gallego-Villada, E.A. Alarcón, A.L. Villa, Effect of Colombian raw materials on the Prins condensation reaction over Sn/MCM-41, Catal. Today 372 (2021) 36–50, https://doi.org/10.1016/j.cattod.2020.10.040.

[80] F. Arena, R. Dario, A. Parmaliana, A characterization study of the surface acidity of solid catalysts by temperature programmed methods, Appl. Catal. Gen. 170 (1998) 127–137, https://doi.org/10.1016/S0926-860X(98)00041-6.

[81] P.Y. Dapsens, C. Mondelli, J. Pérez-Ramírez, Design of Lewis-acid centres in zeolitic matrices for the conversion of renewables, Chem. Soc. Rev. 44 (2015) 7025–7043, https://doi.org/10.1039/C5CS00028A.

[82] P. Wolf, C. Hammond, S. Conrad, I. Hermans, Post-synthetic preparation of Sn-, Ti- and Zr-beta: a facile route to water tolerant, highly active Lewis acidic zeolites, Dalton Trans. 43 (2014) 4514, https://doi.org/10.1039/c3dt52972j.

[83] L.A. Gallego-Villada, E.A. Alarcón, A.L. Villa, Evaluation of nopol production obtained from turpentine oil over Sn/MCM-41 synthesized by wetness impregnation using the Central Composite Design, Mol. Catal. 498 (2020) 111250, https://doi.org/10.1016/j.mcat.2020.111250.

[84] W. Dai, Q. Lei, G. Wu, N. Guan, M. Hunger, L. Li, Spectroscopic signature of Lewis acidic framework and extraframework Sn sites in beta zeolites, ACS Catal. 10 (2020) 14135–14146, https://doi.org/10.1021/acscatal.0c02356.

[85] M. Sánchez-Sánchez, R. van Grieken, D.P. Serrano, J.A. Melero, On the Sn(II) and Sn(IV) incorporation into the AFI-structured AlPO4-based framework: the first significantly acidic SnAPO-5, J. Mater. Chem. 19 (2009) 6833, https://doi.org/10.1039/b905057d.

[86] S. Li, A. Zheng, Y. Su, H. Fang, W. Shen, Z. Yu, L. Chen, F. Deng, Extra-framework aluminium species in hydrated faujasite zeolite as investigated by two-dimensional solid-state NMR spectroscopy and theoretical calculations, Phys. Chem. Chem. Phys. 12 (2010) 3895, https://doi.org/10.1039/b915401a.

[87] C.A. Fyfe, J.L. Bretherton, L.Y. Lam, Solid-state NMR detection, characterization, and quantification of the multiple aluminum environments in US-Y catalysts by 27 Al MAS and MQMAS experiments at very high field, J. Am. Chem. Soc. 123 (2001) 5285–5291, https://doi.org/10.1021/ja003210k.

[88] S.R. Batool, V.L. Sushkevich, J.A. van Bokhoven, Correlating Lewis acid activity to extra-framework aluminum species in zeolite Y introduced by Ion-exchange, J. Catal. 408 (2022) 24–35, https://doi.org/10.1016/j.jcat.2022.02.010.

[89] F. Deng, Y. Yue, C. Ye, Observation of nonframework Al species in zeolite β by solid-state NMR spectroscopy, J. Phys. Chem. B 102 (1998) 5252–5256, https://doi.org/10.1021/jp9801929.

[90] C.A. Fyfe, J.H. O'Brien, H. Strobl, Ultra-high resolution 29Si MAS NMR spectra of highly siliceous zeolites, Nature 326 (1987) 281–283, https://doi.org/10.1038/326281a0.

[91] D.H. Brouwer, Applications of silicon-29 NMR spectroscopy, in: Compr. Inorg. Chem. III, Elsevier, 2023, pp. 107–137, https://doi.org/10.1016/B978-0-12-823144-9.00032-7.

[92] J.E. Sánchez-Velandia, J.A. Castañeda-Olarte, C.F. Imbachí-Gamba, F. Martínez-Ortega, A.L. Villa, Hydrolysis of limonene epoxide over hierarchical zeolites, Catal. Lett. 153 (2023) 150–166, https://doi.org/10.1007/s10562-022-03963-y.

[93] M.F.M. Gunam Resul, A.M. López Fernández, A. Rehman, A.P. Harvey, Development of a selective, solvent-free epoxidation of limonene using hydrogen peroxide and a tungsten-based catalyst, React. Chem. Eng. 3 (2018) 747–756, https://doi.org/10.1039/C8RE00094H.

[94] R. Barrera Zapata, A.L. Villa, C. Montes de Correa, Kinetic modeling of limonene epoxidation over PW-amberlite, Ind. Eng. Chem. Res. 48 (2009) 647–653, https://doi.org/10.1021/ie800822n.

[95] A.J. Bonon, Y.N. Kozlov, J.O. Bahú, R.M. Filho, D. Mandelli, G.B. Shul'pin, Limonene epoxidation with H2O2 promoted by Al2O3: kinetic study, experimental design, J. Catal. 319 (2014) 71–86, https://doi.org/10.1016/j.jcat.2014.08.004.

[96] D.Y. Murzin, Solvent effects in catalysis: implementation for modelling of kinetics, Catal. Sci. Technol. 6 (2016) 5700–5713, https://doi.org/10.1039/C6CY00495D.

[97] V. Gutmann, Solvent effects on the reactivities of organometallic compounds, Coord. Chem. Rev. 18 (1976) 225–255, https://doi.org/10.1016/S0010-8545(00)82045-7.

[98] P.K. Chattopadhyay, B. Kratochvil, Ligand substitution kinetics of nickel(II) ion in N,N -dimethylformamide, Can. J. Chem. 55 (1977) 3449–3455, https://doi.org/10.1139/v77-483.

[99] D.R. Joshi, N. Adhikari, An overview on common organic solvents and their toxicity, J. Pharm. Res. Int. 28 (2019) 1–18, https://doi.org/10.9734/jpri/2019/v28i330203.

[100] C.L. Yaws, Yaws' Thermophysical Properties of Chemicals and Hydrocarbons, Electronic, Knovel, 2010. https://app.knovel.com/hotlink/toc/id:kpYTPCHE02/yaws-thermophysical-properties/yaws-thermophysical-properties.

[101] S. Murov, Properties of Solvents Used in Organic Chemistry, 2020. http://murov.info/orgsolvents.htm. (Accessed 30 July 2023).

[102] M. Díaz, E. Epelde, J. Valecillos, S. Izaddoust, A.T. Aguayo, J. Bilbao, Coke deactivation and regeneration of HZSM-5 zeolite catalysts in the oligomerization of 1-butene, Appl. Catal. B Environ. 291 (2021) 120076, https://doi.org/10.1016/j.apcatb.2021.120076.

[103] M. Boronat, P. Concepción, A. Corma, M. Renz, S. Valencia, Determination of the catalytically active oxidation Lewis acid sites in Sn-beta zeolites, and their optimisation by the combination of theoretical and experimental studies, J. Catal. 234 (2005) 111–118, https://doi.org/10.1016/j.jcat.2005.05.023.

[104] G. Casella, S. Carlotto, A.P.C. Ribeiro, L.M.D.R.S. Martins, The reaction of acetonitrile with hydrogen peroxide in alkaline medium: a DFT mechanistic study of green production of amides, Phys. Chem. Chem. Phys. 25 (2023) 22775–22781, https://doi.org/10.1039/D3CP02024J.